Title

Do Coupled Megathrusts Rupture?

Authors

Bar Oryan*[1] & Alice-Agnes Gabriel[1,2]

Affiliations

(1) Scripps Institution of Oceanography, University of California at San Diego, La Jolla, CA 92093, USA
(2) LMU Munich, Germany

Abstract

Megathrust earthquakes are among the most destructive and least predictable natural hazards. Kinematic geodetic coupling models[1], which identify regions of the plate interface where interseismic strain accumulates, are essential for seismic and tsunami hazard assessment[2–5]. Yet their reliability remains debated: geodetic records are short[6,7], offshore resolution remains poor[8], and earthquake ruptures may propagate dynamically across both creeping and locked slab portions[9–12]. This uncertainty has limited our ability to assess whether large earthquakes release strain where coupling is strongest or rupture independently of interseismic coupling. Here we present the first systematic global analysis of slip-coupling relationships, compiling 61 earthquake slip models (moment magnitude Mw 6.7–9.1) across 12 subduction zones. We show that large earthquakes (Mw ≥ 7.5) consistently concentrate slip in highly coupled regions, whereas smaller events rupture more variably, almost entirely in weakly coupled areas. These results indicate that major earthquakes predominantly release long-term accumulated strain, while smaller events reflect shorter-term heterogeneity, such as transient asperities, motivating time-dependent coupling models that capture evolving fault strength. Our findings reconcile apparent inconsistencies between kinematic coupling models and seismic slip and establish magnitude-dependent controls on earthquake rupture, with direct implications for seismic hazard assessment.

MAIN TEXT

Introduction

The largest earthquakes on Earth occur at subduction zones, where a dense plate sinks into the mantle, sliding below an upper plate[13]. The boundary between these plates, known as the megathrust, contains asperities[14] that remain fixed during the interseismic period, accumulating strain over decades to centuries before rupturing in an earthquake. As strain gradually builds up, the overriding plate deforms, generating surface displacements[15] that are routinely measured by geodetic networks. Kinematic coupling models are essential for assessing seismic and tsunami hazards by identifying such asperities[2–5]. To establish coupling models, geodesists invert surface displacements to identify portions of the megathrust that are creeping (kinematic coupling ~ 0) or fixed (kinematic coupling ~ 1), where slip deficit accumulates relative to plate convergence [1] (Fig. 1).

Despite their widespread use, coupling models rely on assumptions that may misrepresent megathrust locking. They are based on surface displacements recorded over just a few decades, a small fraction of the hundreds to thousands of years spanned by earthquake cycles[6,7], a limitation particularly troubling in light of recent geodetic observations showing that coupling can vary substantially over only a few years[16–20]. Measured interseismic deformation may also reflect viscoelastic deformation of the upper plate[21] or contributions from slow-slip events that can last for decades[22].

In addition, spatial constraints such as limited offshore geodetic coverage reduce the resolution of coupling estimates[23,24]. Deformation near the trench is particularly poorly resolved, leading to large uncertainties in shallow megathrust coupling, where coseismic slip may result in devastating tsunamis[8,25]. Beyond these observational limitations, theoretical and numerical studies suggest that high coupling is not a prerequisite for earthquake rupture. Dynamically propagating slip[26] may penetrate creeping regions while strongly coupled areas may act as rupture barriers[9–12].

A Global Comparison of Coupling and Slip

To address the important question of whether geodetically inferred coupling correlates with, or even predicts, megathrust coseismic slip, we establish systematic coupling-slip relationships. We compile, for the first time, a global geodetic dataset of kinematic coupling models spanning twelve active subduction margins (see Materials and Methods), together with 61 coseismic slip models describing individual megathrust earthquakes that ruptured these margins, with a combined moment magnitude of M_w=470 (Figs. 1 and S1; Table S1; Text S1). Coseismic slip is often represented by finite-fault models[27] that resolve the spatial distribution of slip, and in some cases its temporal evolution, across multiple subfaults spanning the rupture surface (Fig. 2A). Each subfault is assigned a slip or rupture rise time value, inferred from teleseismic, regional seismic, geodetic, satellite, or tsunami observations[28,29].

Point-Based Representation of Slip

To compare interseismic coupling and coseismic slip, we discretize finite-fault slip models into point clouds whose density reflects the slip distribution and sample the coupling field at those locations. For each finite-fault model, we generate samples by distributing points within each subfault, with sample size reflecting subfault slip, area, and a sampling density constant κ (Eq. 1). We aggregate the samples across all subfaults such that the resulting point cloud reproduces the finite-fault slip distribution. As an example, expressing the Mw 7.7 2007 Tocopilla earthquake (Fig. 1A) as sample points shows that the discrete slip-distribution resolution improves with increasing κ and sample count (Fig. 2B1–4). From this point cloud, we assign coupling values to each sample (Figs. 2C1–2), aggregating them into a slip-weighted cumulative distribution function (CDF) describing how slip is distributed across the coupling spectrum. We use CDFs as it avoids additional hyperparameter choices (bin widths or kernel bandwidths required by probability density functions) and it converges quickly toward the underlying coupling–slip distribution, allowing us to use relatively small sample counts to reduce computational costs (Text S2, Figs. S2 and S3). This is nicely demonstrated by the Tocopilla earthquake case, where CDFs computed from widely different sample sizes align, revealing that approximately 60% of the coseismic slip occurred in areas with coupling values below 0.4, and only about 15% in regions where coupling exceeds 0.8 (Fig. 2D).

Quantifying Coupling Model Uncertainty

Coupling models are often ill-constrained, particularly offshore, yet they are usually reported as a single best-fitting solution without explicit uncertainty estimates. We provide first-order assessment of coupling uncertainty by estimating interseismic posterior covariance along all twelve megathrusts. We discretize all twelve subduction interfaces into triangular dislocations based on Slab2 geometries[30] and compute the Green's functions for GNSS stations utilized in the respective original coupling studies to estimate the posterior covariance (Eq. 5). In Chile, for example, the interface is discretized into 151 triangular fault patches with Green's functions calculated for ~300 nearby GNSS stations, yielding interseismic slip uncertainty that ranges from ~50% of the plate convergence rate in poorly resolved regions to ~5% in well-constrained areas (Fig. 2E). Finally, we propagate this interseismic slip uncertainty into 500 realizations of coseismic slip–coupling correlations (methods).

Results

Do Coupled Megathrusts Rupture?

Whether megathrust ruptures align with strongly coupled regions provides a fundamental test of the predictive value of geodetically inferred locking models[31–33]. We systematically test this by discretizing 61 (Fig. S1) earthquakes into ~12.5 million slip points and assigning coupling values according to their position within the twelve corresponding coupling distributions. The resulting

CDF, constructed from the best-fitting coupling models (ignoring uncertainty), shows that 60% of slip occurs where coupling is above 0.7 and 15% is released in fully coupled areas (Fig. 3A). This slip–coupling correlation is stronger than the slow-slip-coupling correlation we compute (Fig. 3A) at the Hikurangi subduction zone (Fig. S4). It is, however, weaker than in idealized seismic cycles simulations we perform, where about half of the slip occurs in fully coupled regions and none at coupling values below ~0.5 (Fig. 3A, Methods). These two end-members bracket plausible behavior but do not, on their own, demonstrate whether megahurst slip genuinely favors coupled regions.

To analyze this quantitatively, we construct a null model in which the spatial association between slip and coupling is completely random. For each megathrust earthquake in our database (each represented by a finite-fault model) we generate 500 synthetic realizations by translating and rotating its slip distribution across the coupling field (Methods). We then build two ensembles for comparison: 500 null realizations from the synthetic events and 500 slip-coupling realizations from the observed earthquakes, reflecting our estimated coupling uncertainty. Across 250,000 evaluations (Eq. 7), the observed distributions exceed the null in more than 90% of cases across the entire coupling spectrum. This supports the conclusion that slip is preferentially concentrated in coupled regions, particularly within the most strongly coupled portions of the interface (Fig. 3A).

Variation in slip–coupling correlation across earthquake magnitudes

Our compilation of earthquake slip models ranges from moderate events to ruptures hundreds of kilometers long, allowing us to analyze whether slip–coupling relationships vary with magnitude. We bin slip samples in ~0.4-magnitude intervals and computing slip–coupling for each group. We observe slip–coupling correlation that strengthens with moment magnitude. For events larger than Mw 8.7, ~55% of slip occurs above coupling of 0.8, whereas for events smaller than Mw 7.5, only ~10% of slip occurs above 0.8 (Fig. 3B). Comparison of each magnitude-binned CDF with their corresponding null model sharpens this contrast. For Mw < 7.1 earthquakes, the observed mean CDF curves exceed 80% of the null below coupling 0.2, but the null dominates at higher values (Fig. 3C1). Mw 7.1–7.5 events show a similar shift, favoring coupled regions up to ~0.55 before the null prevails (Fig. 3C2). Smaller events therefore rupture weakly coupled areas, while largely avoiding strongly coupled regions. By contrast, earthquakes larger than Mw 7.5 mirror the aggregate results (Fig. 3A): their observed slip–coupling correlations exceed the null across the entire spectrum (Fig. 3C3-6) and most of their slip is concentrated in strongly coupled regions (Fig. 3B), a pattern confirmed by bootstrap experiments (Text S6, Fig S13). To analyze whether this magnitude dependence holds at the level of individual events, we compute CDFs for each of the 61 megathrust slip models (Fig. 4A1) and compare them using the Cramér–von Mises distance (CvM; Eq. 3). This metric quantifies the disparity between cumulative distributions and provides

a direct measure of heterogeneity in each event's slip–coupling relationship. Once again, earthquakes below Mw 7.5 emerge as outliers, with average CvM distances about 3.5 times greater than those of larger earthquakes and standard deviations 2.6 times higher (Fig. 4B1). We obtain similar results using an alternative L2 norm distance metric (Fig. S13). We interpret this as evidence that lower-magnitude earthquakes have more heterogeneous slip distributions and less systematic slip–coupling relationships, whereas larger ruptures exhibit consistent correlation of slip and coupled regions.

Variation in slip–coupling correlation across subduction zones

Differences in slip–coupling may reflect contrasts among subduction zones, some of which produce great earthquakes while others host only moderate events[34]. We thus test whether variability across margins shapes the slip–coupling relationship we observed. We compute slip–coupling CDFs for each of the twelve subduction zones (Fig. 4A2) and quantify pairwise disparities using the CvM distance. Chile[35] emerges as the most distinct margin, with an average CvM value of 0.13, more than twice the global mean of 0.06. This reflects both the strongest alignment of slip with highly coupled regions (Fig. 4B1) and the largest CvM distance from other margins (Fig. 4B2). However, because Chile also exhibits the highest baseline kinematic coupling of all margins (Fig. 1), its distinctive signature may primarily reflect elevated coupling rather than a fundamentally different slip–coupling behavior.

To account for such baseline differences, we subtract each margin's null CDF from its observed CDF. This null solution, constructed from synthetic megathrust slip distributions that randomly sample the local coupling field, already encodes baseline coupling; subtracting it isolates the true slip–coupling association. We recompute CvM distances on these residuals and demonstrate it produces a tighter inter-margin cluster. For example, the global mean distance decreases by about half, and Chile drops more than fourfold to 0.03 (Fig. 4B2). This indicates that much of the apparent inter-margin contrast may arise from differences in baseline coupling rather than intrinsically different slip–coupling behavior, a correlation that can be observed using the L2 norm as well (Fig. S14).

The Role of Dynamic Weakening in Slip–Coupling Correlations

Our observations raise the question of whether the weaker slip–coupling correlations, especially for smaller events, can be explained by dynamic rupture processes. Earthquake rupture is inherently dynamic, involving non-linear interactions of seismic waves, rapid fault stress changes, and frictional weakening that unfold within seconds to minutes[10,26,36]. To assess the role of co-seismic dynamic weakening, we compute the probability density function (PDF) of spatiotemporal slip evolution for 25 (out of 61, Mw 6.7-8.4) megathrust earthquakes. We find no systematic influence of dynamic weakening on slip partitioning. Ruptures (Fig S15) concentrate most slip within ±0.2 of the hypocenter's initial coupling and are equally likely to propagate into lower-

coupling regions, which are presumably less critically stressed and may require enhanced dynamic weakening to slip[10], as into higher-coupling regions (Fig. 5A, Fig. S16B). A similar pattern emerges for the corresponding spatiotemporal null solution, where randomized slip–coupling–time correlations results in slip evenly distributed above and below its initial coupling (Fig. 5). Examining this slip-coupling for all 61 megathrusts confirms this result as we find no systematic preference for rupture propagation into either higher or lower coupling across magnitudes (Fig. S17). This contrasts with our rate-and-state friction simulations[37,38], where slip nucleates in fully coupled regions (~1) and preferentially propagates into less coupled areas (Fig. 5).

Discussion and Conclusions

We identify a fundamental distinction in slip-coupling relationships: large megathrust earthquakes rupture strongly coupled regions, whereas moderate events rupture more heterogeneous portions of megathrusts (Fig. 4) that are less critically stressed (Fig. 3). This result is surprising, as many earthquake characteristics are generally assumed to be scale-independent [39] relieving strain that accumulated during the interseismic period[40]. Moderate earthquakes may instead nucleate in regions of lower strain accumulation, failing to build sufficient energy to propagate widely.In the absence of clear evidence for the effects of enhanced dynamic weakening (Figs. 5 & S17), we suggest that smaller events may rupture transient asperities, whereas larger earthquakes rupture more uniform, persistent asperities[14,20].

Consistent with this interpretation, numerical simulations[9] demonstrate that regions with strong heterogeneity in frictional or initial stress properties behave fundamentally differently from uniform asperities. Whereas the latter remain largely persistently coupled until failure, heterogeneous patches show large temporal fluctuations in coupling and strain accumulation, hosting smaller and more variable ruptures. This contrast provides a mechanistic explanation for our observations: large earthquakes may rupture stable asperities that are well resolved in geodetic observations, whereas smaller events rupture transient asperities whose evolving coupling[17,18,20] and strain accumulation remain only partially captured by present datasets.

The same natural complexity that may shape transitional asperities could also govern baseline coupling differences across margins, reflecting the interplay of temperature, rheology, stress, and fluid conditions along different megathrusts[41–44]. This complexity likely explains why slip–coupling correlations in nature appear weaker than in our idealized models that do not capture such heterogeneity (Fig. 3). Crucially, once these baseline effects are accounted for, slip–coupling relationships emerge as broadly consistent across subduction zones (Fig. 4). While our analysis cannot isolate which properties control baseline coupling, it suggests that some margins, such as Chile, host more great earthquakes because interface conditions promote strongly locked, more uniform slip patches, whereas more heterogeneous margins may inhibit the development of such persistent asperities[14].

Resolving whether variability in coupling reflects transient or enduring asperities requires evidence beyond the existent, short geodetic record[20]. Subduction landscapes provide such archives, preserving the cumulative imprint of many interseismic periods through uplifted marine terraces[45], river incision[46], and shelf breaks[47], offering a powerful complement to geodetic datasets[48]. Combining these perspectives can help assess whether variability in coupling reflects transient asperities or enduring features of the megathrust. This question is critical, because even moderate events ($Mw < 7.5$), which our results show are not well constrained by traditional coupling models, can pose major risks to coastal populations[49].

In summary, we present the first global analysis of slip–coupling correlations, providing new constraints on the link between geodetically inferred kinematic coupling patterns and earthquake slip distributions. Across 61 megathrust earthquakes spanning twelve subduction zones, we show that large ruptures ($Mw \geq 7.5$) concentrate slip in strongly coupled regions, whereas smaller events rupture more variably, often in weakly coupled areas. Inter-margin comparisons reveal that once baseline differences in coupling strength are removed, slip–coupling relationships converge to a consistent global pattern. This demonstrates that despite regional variations in convergence rate, slab geometry, sediment supply, and thermal structure, the mechanics connecting coupling and rupture are fundamentally similar across subduction zones.

Materials and Methods

Data selection

To evaluate whether coseismic slip preferentially occurs where the plate interface is most strongly coupled, we assemble a global dataset that pairs interseismic kinematic coupling maps with finite-fault slip models. We highlight that kinematic coupling should not be confused with frictional locking, which describes the fault's mechanical response to slip, where "locked" implies unstable behavior, or with seismic coupling, which measures the fraction of total slip released seismically, with 1 indicating entirely seismic slip [8]

The coupling model portion of our dataset includes twelve subduction margins (Fig. 1), with coupling maps chosen to favor models that use the latest geodetic data and cover the largest area (Text S1). These include the Kamchatka[51], Chile[35], Peru[52], Colombia and Ecuador[53], Mexico[54], Costa-Rica[55], Sumatra[56], Alaska[57,58], Japan[59], Nanaki[60] , Sagami[24] and the Himalayas[61] subduction zones.

For each margin, we compile published finite-fault models locally coinciding with the corresponding coupling region, yielding distinct 61 earthquakes (Mw 6.8–9.2) that occurred between 1923 and 2024 (Fig 1;Fig. S1;Table S1). We rely primarily on slip solutions derived by the USGS based on body- and surface-wave inversions, which reduces methodological variability and extends coverage to many otherwise undocumented megathrust earthquakes [27,62–87]. We supplement our dataset with slip models from other published studies that document slip for historic earthquakes and were made available via the SRCMOD database[50,88–103].

Data sampling

We compare slip distributions with kinematic coupling maps, $C(x, y)$, by sampling each finite-fault model and expressing the slip distribution as a discrete point cloud (Figs. 2B1,D1-4). For each finite-fault model, all subfaults are sampled such that for a given subfault i we draw N_i points uniformly within its bounds, with the number of points proportional to its planar subsurface area A_i, and slip, S_i:

$$N_i = \kappa \cdot A_i S_i \text{ , (1)}$$

Where κ is a density proportionality constant set to 3500 km^{-3} for our primary analysis and 750 km^{-3} for the null and spatial uncertainty analyses. These choices ensure that all 61 CDFs converge, with sampling uncertainties smaller than 1% and 5%, respectively (Text S2 and Fig S2).

Next, we use the surface positions x_j, y_j of each sampling point, j, to evaluate the coupling, $C_j = C(x_j, y_j)$ (e.g., Fig 2B2). The resulting sets of coupling values, $\{C_j\}_{j=0}^{N_f}$, represent a slip-

weighted sampling of the coupling field, modulated by how coseismic slip is distributed across the range of coupling values. We note that for the case where we sample the rupture time (e.g., Fig. 5) we assign a uniform rise time for all samples drawn from subfault i.

Lastly, for simplification, we assume that the geometry of the inverted coupling models and the finite fault models align. Although this may not always be true, correcting geometry discrepancies is challenging. Coupling models rarely provide the geometry employed during their inversion, and reprojecting either finite fault or coupling models onto a different geometry may alter the original inversion and lead to uncertainties [88,99].

Characterizing slip–coupling relationships

We compile all N_t coupling assigned samples, $\{C_q\}_{q=0}^{N_t}$, from the finite-slip models, considering either the full dataset spanning 61 megathrusts (Fig. 3A) or any subset of interest , such as specific earthquakes (Fig. 4A1), subduction-related groups (Fig. 4A2) or selected magnitude ranges (Fig. 3C). Following, we compute the CDFs using:

$$\hat{P}(C) = \frac{1}{N_t} \sum_{q=1}^{N_t} \mathbf{1}_{\{C_q \leq C\}}, \quad (2)$$

where $\mathbf{1}_{\{C_q \leq C\}}$ is the indicator function returning 1 if $C_q < C$ and 0 otherwise.

We compute the distance between two cumulative distribution functions $\hat{P}_1(C)$ and $\hat{P}_2(C)$ using the Cramér-von Mises (CvM) distance:

$$\omega = \int_0^1 \left(\hat{P}_1(C) - \hat{P}_2(C)\right)^2 dC. \quad (3)$$

We evaluate the joint spatiotemporal distribution of slip and coupling by computing a probability density function (PDF) of rupture rise time, T, normalized to 0–1, and coupling ,ΔC, shifted so that the PDF value at the hypocenter is set to 0 and ΔC spans –1 to 1. We use ~700,000 samples from 25 megathrust earthquakes which resolve spatiotemporal slip and employ a kernel density estimator to compute the PDF:

$$\hat{f}(T, \Delta C) = \frac{1}{N_t |H|^{1/2}} \sum_{q=1}^{N_t} \frac{1}{2\pi} \exp\left(-\tfrac{1}{2} \left[H^{-1/2} \begin{bmatrix} T - T_q \\ \Delta C - \Delta C_q \end{bmatrix} \right]^\top \left[H^{-1/2} \begin{bmatrix} T - T_q \\ \Delta C - \Delta C_q \end{bmatrix} \right] \right), \quad (4)$$

where H is a bandwidth matrix defined by $H = N_t^{-1/6} \Sigma^{1/2}$ and Σ is the covariance matrix.

Quantifying spatial uncertainty in coupling fields

We quantify and propagate uncertainty in coupling models using linear inverse theory, where the posterior model covariance, C_{post}, is expressed as [104]:

$$\mathbf{C}_{\text{post}} = \left(\mathbf{G_{hf}}^{\top}\mathbf{C}_n^{-1}\mathbf{G_{hf}} + \alpha^2\mathbf{L}^{\top}\mathbf{L}\right)^{-1}, \quad (5)$$

where G_{hf} is the Green's function that maps the unit slip on a patch h in strike- and dip-slip directions to the corresponding displacement at station f in the east, north and vertical directions, C_n is the data covariance, L is the Laplacian smoothing operator and α is the regularization weight.

We estimate C_{post} for each margin by computing the Green's functions, G_{hf}, for all geodetic observations used in the original studies.We assume an elastic half-space with a Poisson ratio of 0.25 and discretize the twelve subduction margins into twelve uniform meshes of triangular dislocations[105] based on Slab2 geometries[30]. The number of patches is selected such that the available three-component geodetic observations[35] are roughly three times the number of slip parameters in the dip and strike directions. We construct C_n, assuming uncorrelated data uncertainties with standard deviations of 4 mm/yr and 2 mm/yr in the vertical and horizontal directions, respectively. For coupling models based on InSAR[54,55], we assign uncertainties twice larger and represent the observations as stations distributed on a uniform grid with the same density and spatial extent as reported in the original work. Lastly, we apply a regularization weight of α=0.1.

Subsequently, for each subduction we draw five hundred correlated interseismic slip realizations from the multivariate normal distribution $\mathcal{N}(\boldsymbol{S}, \mathbf{C}_{\text{post}})$, bounded[106] between zero and the plate convergence rate S_{cov}[107] where the mean interseismic slip rate, S, is linked to coupling field, C(x,y), and S_{cov}:

$$S(x,y) = S_{\text{cov}}\left(1 - C(x,y)\right). \quad (6)$$

For each slip realization, we compute the corresponding coupling field using Equation (6). We then sample each of the 61 finite fault models against the 500 coupling realizations to obtain a distribution of slip–coupling correlations, which we use to compute the deviation from our mean slip-coupling correlation. We acknowledge that our discretization choices and regularization parameters may differ from those in the original coupling models. Our goal here, however, is to provide first-order estimates consistent across all subductions rather than strictly reproducing the original inversions. We also do not account for other sources of nonuniqueness, such as uncertainties in cosesmic slip models (Text S3, Figs S5-7, Table S2-S3), the influence of smoothing constraints (Text S4, Figs. S8-9), and differences among coupling models (Text S5, Fig. S10)

Null model

We assess whether the observed correlation between slip and coupling is significant by constructing a null model in which their spatial association is purely random. For each of the 61 megathrust earthquakes, we generate 500 synthetic realizations, resulting in 30,500 null earthquake slip models spreading across ~1.2 billion samples. For each realization, we translate the original finite fault model to a location drawn uniformly within the subduction margin where the original megathrust earthquake model ruptured. We then rotate the model about a pivot point chosen at random within the projected realization, with an angle drawn uniformly from 0 to 360 degrees. We only retain synthetic earthquake models for which at least 95% of slip samples fall within regions where coupling is defined. We preserve the original finite-fault downdip orientation and ignore geometric discrepancies between the coupling model and accepted realizations.

We accept the hypothesis that slip favors coupling up to level c if the observed CDFs, $\mathrm{CDF}^{\mathrm{obs}}$, exceed the null CDFs, $\mathrm{CDF}^{\mathrm{null}}$, in more than half of the pairwise comparisons:

$$H(c) \;=\; \frac{1}{500 \times 500} \sum_{i=1}^{500} \sum_{j=1}^{500} \mathbf{1}\big[\, CDF_i^{\mathrm{obs}}(c) \;>\; CDF_j^{\mathrm{null}}(c) \,\big] \quad (7)$$

Slip-coupling correlation for idealised quasi-dynamic megathursts

We simulate sequences of earthquakes and aseismic slip[108] on an idealised megathrust interface using the open-source code Tandem[109,110]. Our 2D volumetric model domain is homogeneous and spans 4500 km in width and 400 km in depth, and is intersected by a megathrust dipping at 10 degrees (Fig. S9C). We impose backslip boundary conditions, allowing the deeper portion of the fault below 40 km to slip freely at a rate V_{pl}[40,109]. The system evolves temporally by solving for the slip velocity, V, and the state variable,θ, along the megathrust, which obeys the regularized formulation of rate-and-state friction [111]:

$$F(V,\theta) = a \sinh^{-1}\left[\frac{\|V\|}{2V_0} \exp\left(\frac{f_0 + b \cdot \ln\left(V_0\theta/D_{RS}\right)}{a}\right)\right], \quad (8)$$

Where D_{RS} is the characteristic state evolution distance, a,b are friction parameters describing the direct and evolution effects, and f_0 and V_0 are the reference velocity and friction coefficient, and the evolution of the state variable, θ, adheres to the aging law[37,38] :

$$\frac{d\theta}{dt} = 1 - \frac{\|V\|\theta}{D_{RS}} \quad (9)$$

We use our simulated interseismic period and estimate kinematic coupling along fault nodes, $C_t(x)$, using:

$$C_t(x) = 1 - \frac{s(x, t_{eq}) - s(x, t_{40})}{V_{\mathrm{pl}}\,(t_{eq} - t_{40})} \quad (10)$$

where $s(x, t_{eq})$ and $s(x, t_{40})$ are the cumulative slip at location x at the earthquake onset and 40 years prior (Fig. S12A,B). Coseismic slip is computed similarly. We note that these simulations generate many megathrust earthquakes, however, following the initial spin-up phase, these events become quasi-periodic and consistent allowing us to conduct our analysis on a single representative event (Fig. S12A,B) which happens after 4800 years. See Table S4 for a complete description of model parameters.

Acknowledgements: We thank (in alphabetical order) M. Chlieh, B. Cosenza-Muralles, L. Dal Zilio, C. DeMets, A. Ellis, L. Feng, J. Freymueller, R. Bürgmann, R. Hanifa, G. Hilley, J. Loveless, B. Lovery, L. Maubant, M. Métois, T. Nishimura, D. Panda, R. Plata-Martinez, M. Radiguet, and L. Xue for sharing their coupling models with us. BO and AAG acknowledge the IGPP Green Foundation, National Science Foundation(grant no. OAc-2311208) and CRESCENT Award 2017Y0SD for their support. AAG acknowledges additional support by Horizon Europe (ChEESE-2P, grant number 101093038 and Geo-INQUIRE, grant number 101058518), the National Science Foundation (grant nos. OAC-2139536, OAC-2311208, EAR-2225286, EAR-2121568).

Data availability: Coupling models, finite fault models, slip samples and code to sample finite fault models can be found at 10.5281/zenodo.17160782. Finite-slip models in our dataset were obtained from the SRCMOD database[50] and the USGS.

Competing interest declaration: The authors declare no competing interests.

Author contributions: Conceptualization: B.O., A.A.G.; Data curation: B.O.; Formal analysis: B.O.; Methodology: B.O.; Validation: B.O., A.A.G.; Supervision: A.A.G.; Visualization: B.O.; Funding acquisition: B.O., A.A.G.; Writing – original draft: B.O., A.A.G.; Writing – review & editing: B.O., A.A.G.

Figures

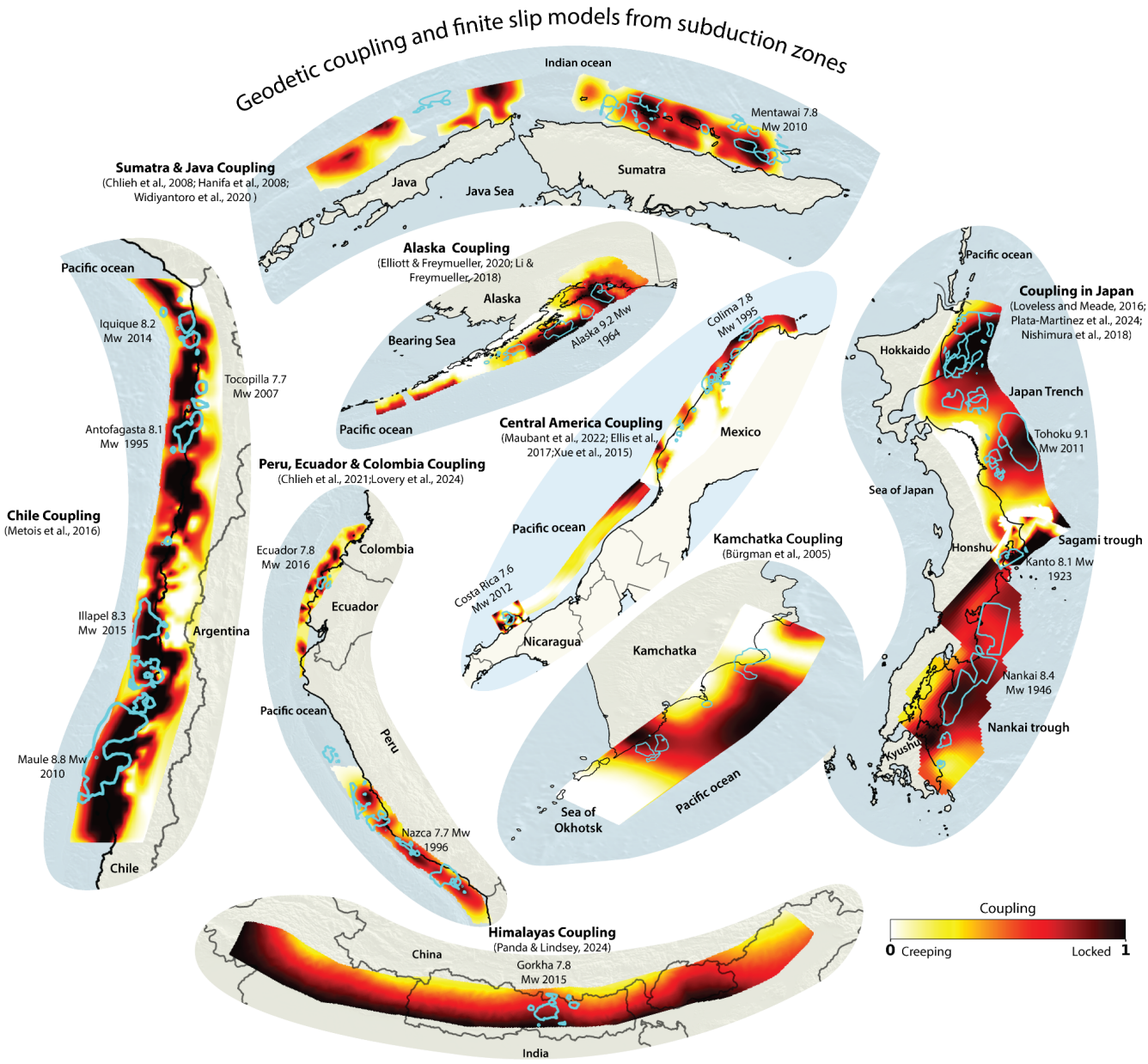

Figure 1 – Twelve subduction zones showing our preferred coupling models together with 61 megathrust earthquake finite fault models. The colormap illustrates interseismic slip rate on the megathrust interface relative to plate convergence rate, with black indicating fully coupled and white and creeping regions. Contours outline areas where coseismic slip is greater than 0.3 × the maximum slip of each event.

.

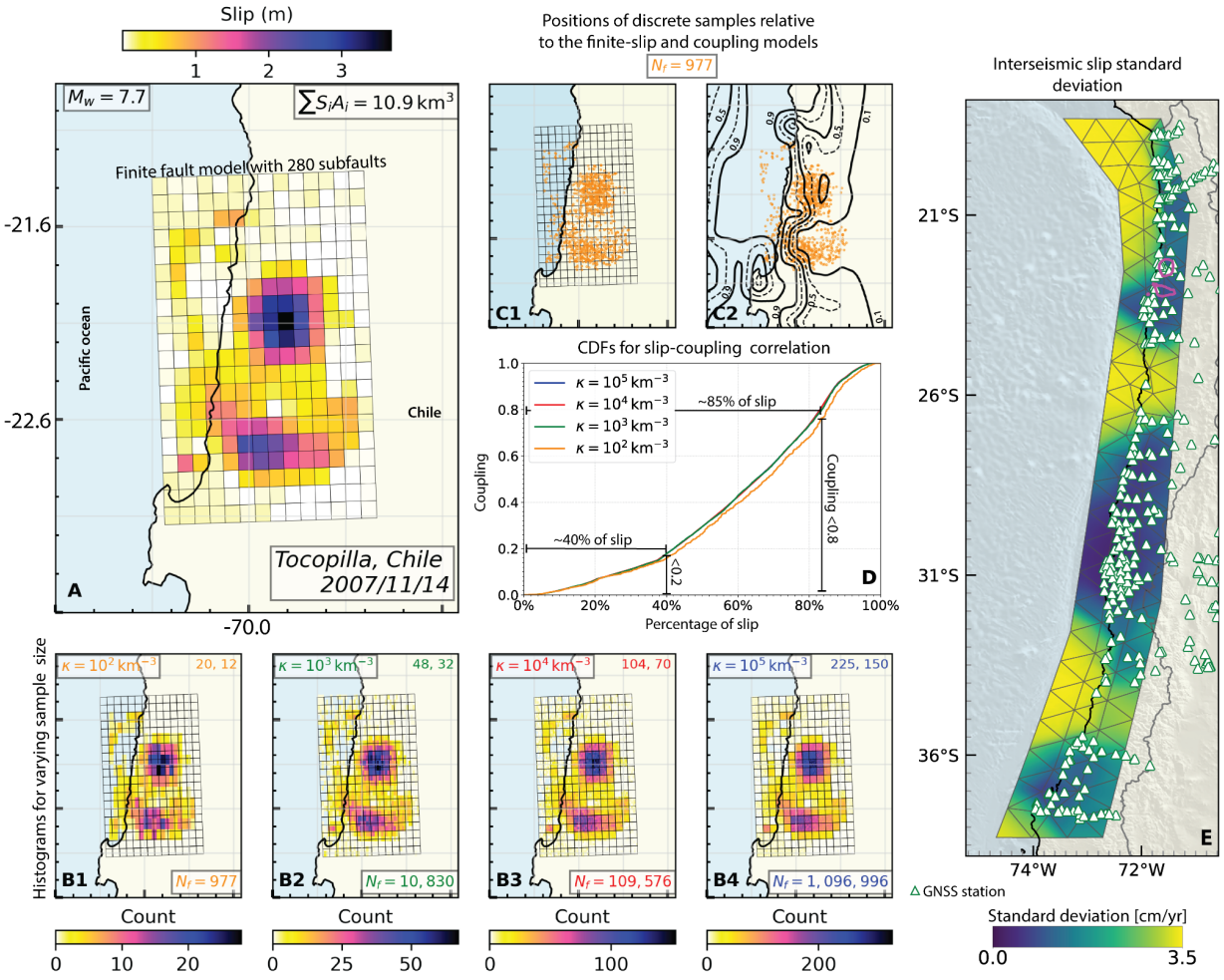

Figure 2 - Coseismic slip distribution and point-based discretization of the 2007 Mw 7.7 Tocopilla megathrust earthquake[27] A – Coseismic slip resolved on 280 rectangular subfaults. B1–B4 - Bin counts along the fault interface, with the number of bins determined by the Freedman–Diaconis rule[112] and shown in the upper right of all panels. C1-C2 – Point-based representation of slip. Dots indicate 977 samples drawn. In C2, contours show the coupling distribution[35] used to assign coupling values to each sample. D – Cumulative distribution functions (CDFs) of slip-coupling correlation for varying κ and sample count. E- Standard deviation of interseismic slip along the megathrust. Green triangles mark GNSS stations, black lines 151 fault patches, and magenta contours the Tocopilla rupture area.

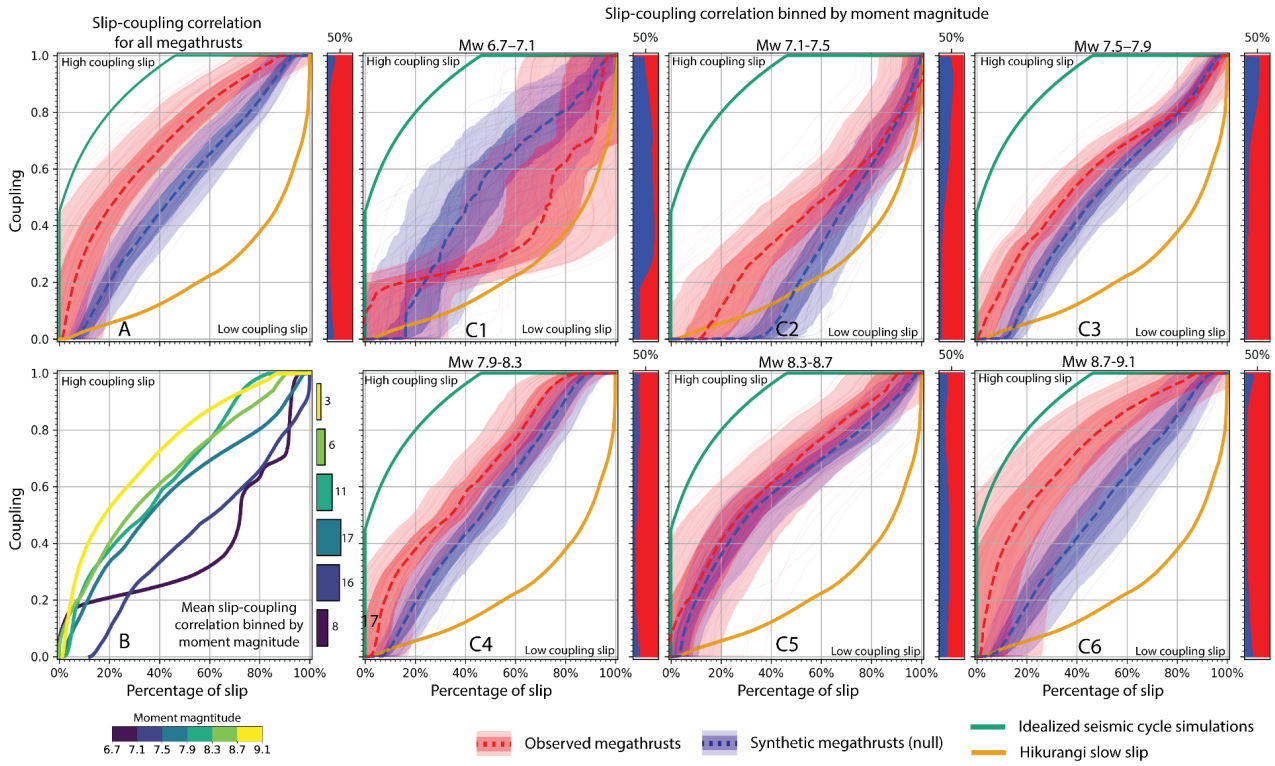

403

404 **Figure 3 - Slip–coupling correlations for observed (red) and synthetic null (blue) megathrust**
405 **earthquakes.** Dashed lines mark the mean distributions from 500 observed slip–coupling
406 realizations incorporating our coupling uncertainty estimates and 500 null realizations with
407 randomized slip–coupling patterns. Shaded bands indicate where 50% and 95% of realizations lie,
408 and 50 random realizations are drawn as faint lines. Marginal bars indicate the percentage of
409 500×500 pairwise comparisons in which observed slip exceeds (red) or falls below (blue) the null.
410 Slip–coupling correlations from seismic cycle simulations and from slow slip at the Hikurangi
411 subduction zone are shown in green and orange, respectively. A – All events combined. B – Mean
412 CDFs for six magnitude bins, with event counts per bin shown by bars. C1–C6 – Full distributions
413 for each magnitude bin.

414

415

416

417

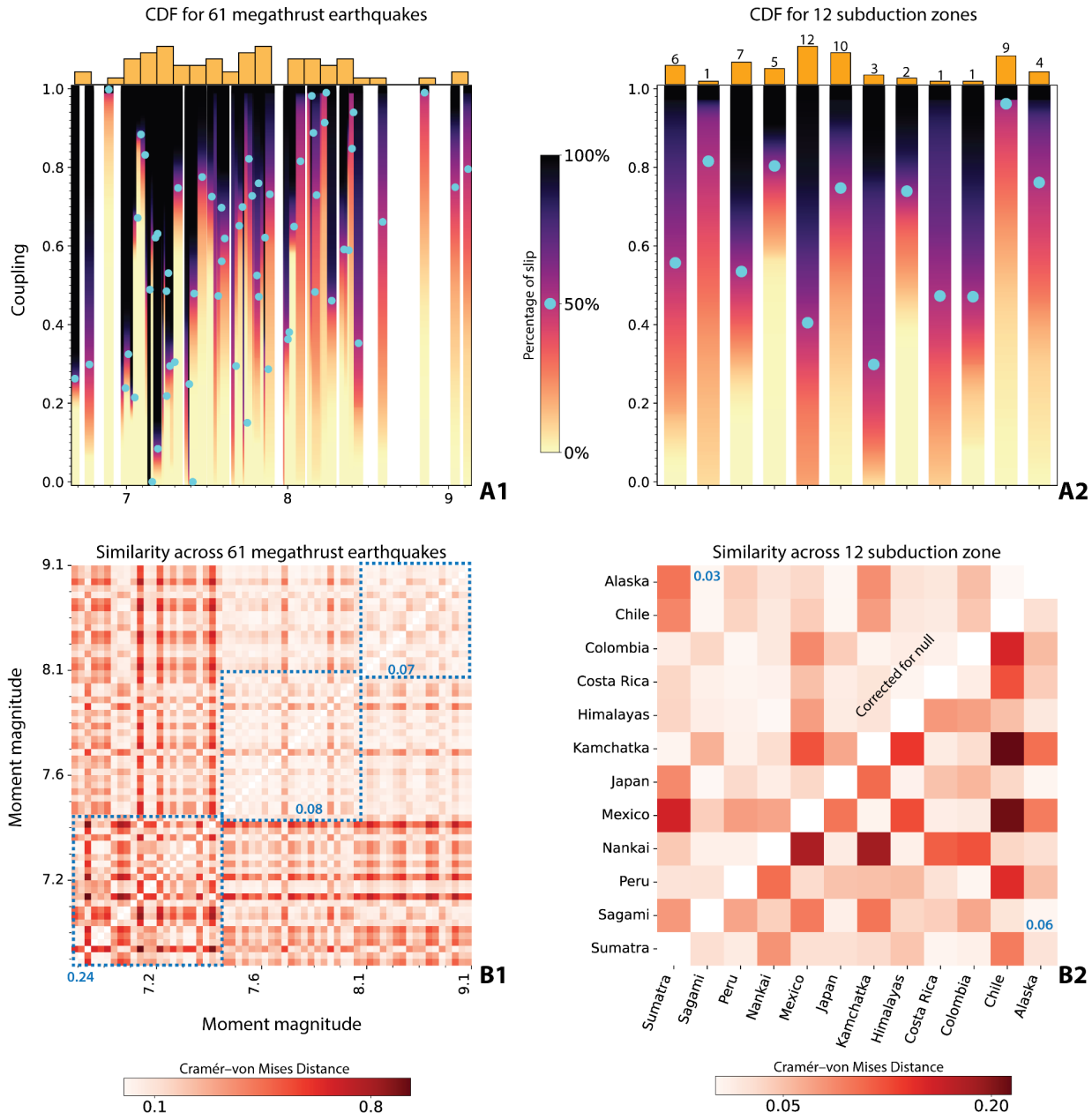

Figure 4. Slip–coupling similarities across megathrust earthquakes and subduction margins. A1- CDFs for 61 observed megathrust earthquakes, with bars showing event counts per 0.1 magnitude bin A2 - CDFs aggregated across 12 subduction zones with bars indicating event counts per margin. B1 - Pairwise Cramér-von-Mises (CvM) distances among the 61 megathrust earthquakes; blue numbers denote mean within-box values. B2 - Pairwise CvM distances among the 12 margins; blue numbers give mean distances for both null-corrected and uncorrected cases.

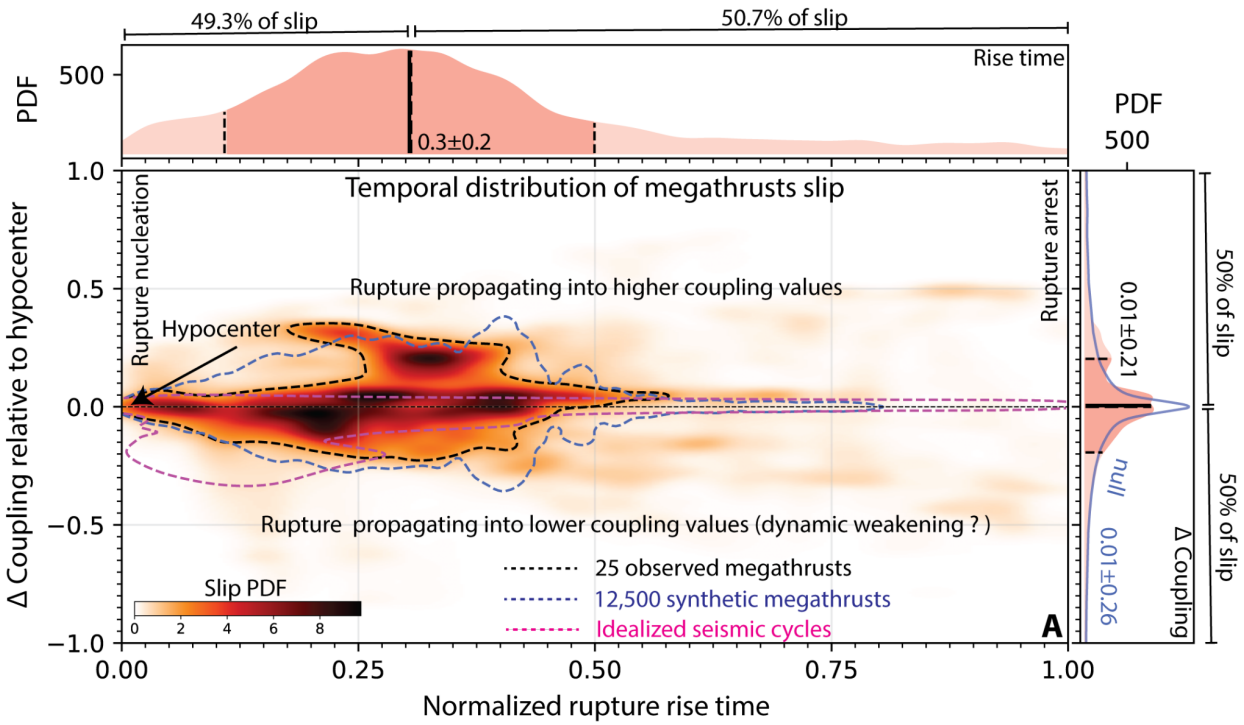

426

427 **Figure 5. Spatiotemporal patterns of megathrust slip.** Probability density of slip versus
428 normalized rupture rise time and coupling relative to the hypocenter for 25 megathrust
429 earthquakes. Black dashed lines enclose 68% of observed slip, while blue and magenta dashed
430 lines mark the same regions for synthetic and simulated events. Marginal panels show PDFs of
431 coupling and rise time, with means (solid lines) and standard deviations (dashed lines).

432

433

References

1. Wallace, L. M., Beavan, J., McCaffrey, R. & Darby, D. Subduction zone coupling and tectonic block rotations in the North Island, New Zealand. *Journal of Geophysical Research: Solid Earth* **109**, (2004).
2. Glehman, J. *et al.* Partial ruptures governed by the complex interplay between geodetic slip deficit, rigidity, and pore fluid pressure in 3D Cascadia dynamic rupture simulations. *Seismica* **2**, (2025).
3. Ramos, M. D. *et al.* Assessing Margin-Wide Rupture Behaviors Along the Cascadia Megathrust With 3-D Dynamic Rupture Simulations. *Journal of Geophysical Research: Solid Earth* **126**, e2021JB022005 (2021).
4. Small, D. T. & Melgar, D. Geodetic Coupling Models as Constraints on Stochastic Earthquake Ruptures: An Example Application to PTHA in Cascadia. *Journal of Geophysical Research: Solid Earth* **126**, e2020JB021149 (2021).
5. Wang, L., Hainzl, S. & Mai, P. M. Quantifying slip balance in the earthquake cycle: Coseismic slip model constrained by interseismic coupling. *Journal of Geophysical Research: Solid Earth* **120**, 8383–8403 (2015).
6. Marco, S. & Klinger, Y. Review of On-Fault Palaeoseismic Studies Along the Dead Sea Fault. in *Dead Sea Transform Fault System: Reviews* (eds Garfunkel, Z., Ben-Avraham, Z. & Kagan, E.) 183–205 (Springer Netherlands, Dordrecht, 2014). doi:10.1007/978-94-017-8872-4_7.
7. Ruiz, S. & Madariaga, R. Historical and recent large megathrust earthquakes in Chile. *Tectonophysics* **733**, 37–56 (2018).
8. Lindsey, E. O. *et al.* Slip rate deficit and earthquake potential on shallow megathrusts. *Nat.*

Geosci. **14**, 321–326 (2021).

9. Molina-Ormazabal, D., Ampuero, J.-P. & Tassara, A. Diverse slip behaviour of velocity-weakening fault barriers. *Nat. Geosci.* 1–8 (2023) doi:10.1038/s41561-023-01312-1.

10. Noda, H. & Lapusta, N. Stable creeping fault segments can become destructive as a result of dynamic weakening. *Nature* **493**, 518–521 (2013).

11. Ramos, M. D. & Huang, Y. How the Transition Region Along the Cascadia Megathrust Influences Coseismic Behavior: Insights From 2-D Dynamic Rupture Simulations. *Geophysical Research Letters* **46**, 1973–1983 (2019).

12. Rubino, V., Lapusta, N. & Rosakis, A. J. Intermittent lab earthquakes in dynamically weakening fault gouge. *Nature* **606**, 922–929 (2022).

13. Bilek, S. L. & Lay, T. Subduction zone megathrust earthquakes. *Geosphere* **14**, 1468–1500 (2018).

14. Lay, T. & Kanamori, H. An Asperity Model of Large Earthquake Sequences. in *Earthquake Prediction* 579–592 (American Geophysical Union (AGU), 1981). doi:10.1029/ME004p0579.

15. Wang, K., Hu, Y. & He, J. Deformation cycles of subduction earthquakes in a viscoelastic Earth. *Nature* **484**, 327–332 (2012).

16. Luo, H. *et al.* A recent increase in megathrust locking in the southernmost rupture area of the giant 1960 Chile earthquake. *Earth and Planetary Science Letters* **537**, 116200 (2020).

17. Marill, L. *et al.* Fourteen-Year Acceleration Along the Japan Trench. *Journal of Geophysical Research: Solid Earth* **126**, e2020JB021226 (2021).

18. Materna, K., Bartlow, N., Wech, A., Williams, C. & Bürgmann, R. Dynamically Triggered Changes of Plate Interface Coupling in Southern Cascadia. *Geophys. Res. Lett.* **46**, 12890–

12899 (2019).

19. Maubant, L., Frank, W. B., Wallace, L. M., Williams, C. A. & Hamling, I. Imaging the Spatiotemporal Evolution of Plate Coupling With Interferometric Radar (InSAR) in the Hikurangi Subduction Zone. *Geophysical Research Letters* **50**, e2023GL105388 (2023).

20. Tsang, L. L. H., Meltzner, A. J., Hill, E. M., Freymueller, J. T. & Sieh, K. A paleogeodetic record of variable interseismic rates and megathrust coupling at Simeulue Island, Sumatra. *Geophysical Research Letters* **42**, 10,585-10,594 (2015).

21. Chong, J.-H., Oryan, B., Shen, L., Steckler, M. S. & Lindsey, E. O. Interseismic Uplift of Anticlines Above the Rakhine-Bangladesh Megathrust From ALOS-2 InSAR. (2024) doi:10.1029/2024JB030003.

22. Mallick, R. *et al.* Long-lived shallow slow-slip events on the Sunda megathrust. *Nat. Geosci.* **14**, 327–333 (2021).

23. DeSanto, J. B., Schmidt, D. A., Zumberge, M., Sasagawa, G. & Chadwell, C. D. Near full locking on the shallow megathrust of the central Cascadia subduction zone revealed by GNSS-Acoustic. *Earth and Planetary Science Letters* **665**, 119463 (2025).

24. Nishimura, T., Yokota, Y., Tadokoro, K. & Ochi, T. Strain partitioning and interplate coupling along the northern margin of the Philippine Sea plate, estimated from Global Navigation Satellite System and Global Positioning System-Acoustic data. *Geosphere* **14**, 535–551 (2018).

25. Almeida, R. *et al.* Can the Updip Limit of Frictional Locking on Megathrusts Be Detected Geodetically? Quantifying the Effect of Stress Shadows on Near-Trench Coupling. *Geophysical Research Letters* **45**, 4754–4763 (2018).

26. Rice, J. R. Heating and weakening of faults during earthquake slip. *Journal of Geophysical*

Research: Solid Earth **111**, 1–29 (2006).

27. Hayes, G. P. The finite, kinematic rupture properties of great-sized earthquakes since 1990. *Earth and Planetary Science Letters* **468**, 94–100 (2017).

28. Ide, S. 4.07 - Slip Inversion. in *Treatise on Geophysics* (ed. Schubert, G.) 193–223 (Elsevier, Amsterdam, 2007). doi:10.1016/B978-044452748-6.00068-7.

29. Wong, J. W. C., Fan, W. & Gabriel, A.-A. A Quantitative Comparison and Validation of Finite-Fault Models: The 2011 Tohoku-Oki Earthquake. *Journal of Geophysical Research: Solid Earth* **129**, e2024JB029212 (2024).

30. Hayes, G. P. *et al.* Slab2, a comprehensive subduction zone geometry model. *Science* **362**, 58–61 (2018).

31. Barnhart, W. D. *et al.* Coseismic slip and early afterslip of the 2015 Illapel, Chile, earthquake: Implications for frictional heterogeneity and coastal uplift. *Journal of Geophysical Research: Solid Earth* **121**, 6172–6191 (2016).

32. Moreno, M., Rosenau, M. & Oncken, O. 2010 Maule earthquake slip correlates with pre-seismic locking of Andean subduction zone. *Nature* **467**, 198–202 (2010).

33. Protti, M. *et al.* Nicoya earthquake rupture anticipated by geodetic measurement of the locked plate interface. *Nature Geosci* **7**, 117–121 (2014).

34. Wirth, E. A., Sahakian, V. J., Wallace, L. M. & Melnick, D. The occurrence and hazards of great subduction zone earthquakes. *Nat Rev Earth Environ* **3**, 125–140 (2022).

35. Métois, M., Vigny, C. & Socquet, A. Interseismic Coupling, Megathrust Earthquakes and Seismic Swarms Along the Chilean Subduction Zone (38°–18°S). *Pure Appl. Geophys.* **173**, 1431–1449 (2016).

36. Sibson, R. H. Interactions between Temperature and Pore-Fluid Pressure during Earthquake

Faulting and a Mechanism for Partial or Total Stress Relief. *Nature Physical Science* (1973) doi:10.1038/physci243066a0.

37. Ruina, A. Slip instability and state variable friction laws. *Journal of Geophysical Research: Solid Earth* **88**, 10359–10370 (1983).

38. Dieterich, J. H. Modeling of rock friction 1. Experimental results and constitutive equations. in *Journal of Geophysical Research: Solid Earth* vol. 84 2161–2168 (1979).

39. Aki, K. Scaling law of seismic spectrum. *Journal of Geophysical Research (1896-1977)* **72**, 1217–1231 (1967).

40. Savage, J. C. A dislocation model of strain accumulation and release at a subduction zone. *Journal of Geophysical Research* (1983) doi:10.1029/JB088iB06p04984.

41. Bassett, D., Shillington, D. J., Wallace, L. M. & Elliott, J. L. Variation in slip behaviour along megathrusts controlled by multiple physical properties. *Nat. Geosci.* **18**, 20–31 (2025).

42. Bürgmann, R. The geophysics, geology and mechanics of slow fault slip. *Earth and Planetary Science Letters* **495**, 112–134 (2018).

43. Gao, X. & Wang, K. Rheological separation of the megathrust seismogenic zone and episodic tremor and slip. *Nature* **543**, 416–419 (2017).

44. Saffer, D. M. & Tobin, H. J. Hydrogeology and Mechanics of Subduction Zone Forearcs: Fluid Flow and Pore Pressure. *Annu. Rev. Earth Planet. Sci.* **39**, 157–186 (2011).

45. Jolivet, R. *et al.* Interseismic loading of subduction megathrust drives long term uplift in northern Chile. 1–21 (2020) doi:10.1029/2019GL085377.

46. Meade, B. J. The signature of an unbalanced earthquake cycle in Himalayan topography? *Geology* **38**, 987–990 (2010).

47. Malatesta, L. C., Bruhat, L., Finnegan, N. J. & Olive, J.-A. L. Co-location of the Downdip End of Seismic Coupling and the Continental Shelf Break. *Journal of Geophysical Research: Solid Earth* **126**, e2020JB019589 (2021).
48. Oryan, B. *et al.* Megathrust locking encoded in subduction landscapes. *Science Advances* **10**, eadl4286 (2024).
49. Sallarès, V. *et al.* Large slip, long duration, and moderate shaking of the Nicaragua 1992 tsunami earthquake caused by low near-trench rock rigidity. *Science Advances* **7**, eabg8659 (2021).
50. Mai, P. M. & Thingbaijam, K. K. S. SRCMOD: An Online Database of Finite-Fault Rupture Models. *Seismological Research Letters* **85**, 1348–1357 (2014).
51. Bürgmann, R. *et al.* Interseismic coupling and asperity distribution along the Kamchatka subduction zone. *Journal of Geophysical Research: Solid Earth* **110**, (2005).
52. Lovery, B. *et al.* Heterogeneous Locking and Earthquake Potential on the South Peru Megathrust From Dense GNSS Network. *Journal of Geophysical Research: Solid Earth* **129**, e2023JB027114 (2024).
53. Chlieh, M. *et al.* Seismic and Aseismic Cycle of the Ecuador–Colombia Subduction Zone. *Front. Earth Sci.* **9**, (2021).
54. Maubant, L. *et al.* Interseismic coupling along the Mexican subduction zone seen by InSAR and GNSS. *Earth and Planetary Science Letters* **586**, 117534 (2022).
55. Xue, L., Schwartz, S., Liu, Z. & Feng, L. Interseismic megathrust coupling beneath the Nicoya Peninsula, Costa Rica, from the joint inversion of InSAR and GPS data. *Journal of Geophysical Research: Solid Earth* **120**, 3707–3722 (2015).
56. Chlieh, M., Avouac, J. P., Sieh, K., Natawidjaja, D. H. & Galetzka, J. Heterogeneous

coupling of the Sumatran megathrust constrained by geodetic and paleogeodetic measurements. *Journal of Geophysical Research: Solid Earth* **113**, (2008).

57. Li, S. & Freymueller, J. T. Spatial Variation of Slip Behavior Beneath the Alaska Peninsula Along Alaska-Aleutian Subduction Zone. *Geophysical Research Letters* **45**, 3453–3460 (2018).

58. Elliott, J. & Freymueller, J. T. A Block Model of Present-Day Kinematics of Alaska and Western Canada. *Journal of Geophysical Research: Solid Earth* **125**, e2019JB018378 (2020).

59. Loveless, J. P. & Meade, B. J. Two decades of spatiotemporal variations in subduction zone coupling offshore Japan. *Earth and Planetary Science Letters* **436**, 19–30 (2016).

60. Plata-Martinez, R. *et al.* Revisiting Slip Deficit Rates and Its Insights Into Large and Slow Earthquakes at the Nankai Subduction Zone. *Journal of Geophysical Research: Solid Earth* **129**, e2023JB027942 (2024).

61. Panda, D. & Lindsey, E. O. Overriding Plate Deformation Controls Inferences of Interseismic Coupling Along the Himalayan Megathrust. *JGR Solid Earth* **129**, e2024JB029819 (2024).

62. USGS. M 7.2 - 106 km S of Sand Point, Alaska. https://earthquake.usgs.gov/earthquakes/eventpage/us7000kg30/finite-fault (2023).

63. USGS. M 7.8 - 99 km SSE of Perryville, Alaska. https://earthquake.usgs.gov/earthquakes/eventpage/us7000asvb/finite-fault (2020).

64. USGS. M 8.2 - Alaska Peninsula. https://earthquake.usgs.gov/earthquakes/eventpage/ak0219neiszm/finite-fault (2021).

65. USGS. M 6.8 - 86 km NW of Vallenar, Chile.

https://earthquake.usgs.gov/earthquakes/eventpage/us7000bfjr/finite-fault (2020).

66. USGS. M 6.9 - 40 km W of Valparaíso, Chile.
https://earthquake.usgs.gov/earthquakes/eventpage/us10008kce/finite-fault (2018).

67. USGS. M 7.7 - 53 km SW of Iquique, Chile.
https://earthquake.usgs.gov/earthquakes/eventpage/usc000p27i/finite-fault (2018).

68. USGS. M 8.0 - 36 km NNE of Antofagasta, Chile.
https://earthquake.usgs.gov/earthquakes/eventpage/usp000714t/finite-fault (2018).

69. USGS. M 7.7 - 83 km SSW of Corinto, Nicaragua.
https://earthquake.usgs.gov/earthquakes/eventpage/usp0005ddn/finite-fault (2018).

70. USGS. M 7.1 - 73 km ENE of Namie, Japan.
https://earthquake.usgs.gov/earthquakes/eventpage/us6000dher/finite-fault (2021).

71. USGS. M 7.2 - 66 km ESE of Ishinomaki, Japan.
https://earthquake.usgs.gov/earthquakes/eventpage/usp000dxe2/finite-fault (2018).

72. USGS. M 7.3 - 57 km ENE of Namie, Japan.
https://earthquake.usgs.gov/earthquakes/eventpage/us6000h519/finite-fault (2022).

73. USGS. M 7.3 - 120 km SE of ?funato, Japan.
https://earthquake.usgs.gov/earthquakes/eventpage/usp000hvhj/finite-fault (2018).

74. USGS. M 7.0 - 102 km E of Petropavlovsk-Kamchatsky, Russia.
https://earthquake.usgs.gov/earthquakes/eventpage/us7000n7n8/finite-fault (2024).

75. USGS. M 7.3 - 187 km SE of Ust'-Kamchatsk Staryy, Russia.
https://earthquake.usgs.gov/earthquakes/eventpage/us2000ivfw/finite-fault (2018).

76. USGS. M 7.5 - 97 km ESE of Ozernovskiy, Russia.
https://earthquake.usgs.gov/earthquakes/eventpage/usp0005u7b/finite-fault (2018).

77. USGS. M 7.8 - 156 km S of Ust'-Kamchatsk Staryy, Russia. https://earthquake.usgs.gov/earthquakes/eventpage/usp0008btk/finite-fault (2018).
78. USGS. M 7.2 - 4 km S of Pinotepa de Don Luis, Mexico. https://earthquake.usgs.gov/earthquakes/eventpage/us2000d3km/finite-fault (2018).
79. USGS. M 7.2 - 9 km ENE of Coyuquilla Norte, Mexico. https://earthquake.usgs.gov/earthquakes/eventpage/usb000pq41/finite-fault (2018).
80. USGS. M 7.4 - 9 km SE of Santa María Xadani, Mexico. https://earthquake.usgs.gov/earthquakes/eventpage/us6000ah9t/finite-fault (2020).
81. USGS. M 7.6 - 35 km SSW of Aguililla, Mexico. https://earthquake.usgs.gov/earthquakes/eventpage/us7000i9bw/finite-fault (2022).
82. USGS. M 7.1 - 37 km W of Atiquipa, Peru. https://earthquake.usgs.gov/earthquakes/eventpage/us2000cjfy/finite-fault (2018).
83. USGS. M 7.2 - 10 km WSW of Atiquipa, Peru. https://earthquake.usgs.gov/earthquakes/eventpage/us6000n8tq/finite-fault (2024).
84. USGS. M 7.6 - 51 km SW of Punta de Bombón, Peru. https://earthquake.usgs.gov/earthquakes/eventpage/usp000aj40/finite-fault (2018).
85. USGS. M 8.4 - 6 km SSW of Atico, Peru. https://earthquake.usgs.gov/earthquakes/eventpage/official20010623203314130_33/finite-fault (2018).
86. USGS. M 7.1 - 171 km SSE of Teluk Dalam, Indonesia. https://earthquake.usgs.gov/earthquakes/eventpage/us7000jvl3/finite-fault (2023).
87. USGS. M 7.4 - 50 km NW of Sinabang, Indonesia. https://earthquake.usgs.gov/earthquakes/eventpage/usp000bfuz/finite-fault (2018).

88. Baba, T., Tanioka, Y., Cummins, P. R. & Uhira, K. The slip distribution of the 1946 Nankai earthquake estimated from tsunami inversion using a new plate model. *Physics of the Earth and Planetary Interiors* **132**, 59–73 (2002).

89. Courboulex, F., Santoyo, M. A., Pacheco, J. F. & Singh, S. K. The 14 September 1995 (M = 7.3) Copala, Mexico, earthquake: A source study using teleseismic, regional, and local data. *Bulletin of the Seismological Society of America* **87**, 999–1010 (1997).

90. Hartzell, S. & Langer, C. Importance of model parameterization in finite fault inversions: Application to the 1974 M 8.0 Peru Earthquake. *Journal of Geophysical Research: Solid Earth* **98**, 22123–22134 (1993).

91. Ichinose, G., Somerville, P., Thio, H. K., Graves, R. & O'Connell, D. Rupture process of the 1964 Prince William Sound, Alaska, earthquake from the combined inversion of seismic, tsunami, and geodetic data. *J. Geophys. Res.* **112**, 2006JB004728 (2007).

92. Ichinose, G. A., Thio, H. K., Somerville, P. G., Sato, T. & Ishii, T. Rupture process of the 1944 Tonankai earthquake (M 8.1) from the inversion of teleseismic and regional seismograms. *Journal of Geophysical Research: Solid Earth* **108**, (2003).

93. Kobayashi, H., Koketsu, K., Miyake, H. & Kanamori, H. Similarities and Differences in the Rupture Processes of the 1952 and 2003 Tokachi-Oki Earthquakes. *JGR Solid Earth* **126**, e2020JB020585 (2021).

94. Kobayashi, R. & Koketsu, K. Source process of the 1923 Kanto earthquake inferred from historical geodetic, teleseismic, and strong motion data. *Earth, Planets and Space* **57**, 261–270 (2005).

95. Mendoza, C. Coseismic slip of two large Mexican earthquakes from teleseismic body waveforms: Implications for asperity interaction in the Michoacan Plate Boundary

Segment. *Journal of Geophysical Research: Solid Earth* **98**, 8197–8210 (1993).

96. Mendoza, C. Finite-fault analysis of the 1979 March 14 Petatlan, Mexico, earthquake using teleseismic P waveforms. *Geophysical Journal International* **121**, 675–683 (1995).

97. Mendoza, C., Hartzell, S. & Monfret, T. Wide-band analysis of the 3 March 1985 central Chile earthquake: Overall source process and rupture history. *Bulletin of the Seismological Society of America* **84**, 269–283 (1994).

98. Mendoza, C. & Hartzell, S. H. Slip distribution of the 19 September 1985 Michoacan, Mexico, earthquake: Near-source and teleseismic constraints. *Bulletin of the Seismological Society of America* **79**, 655–669 (1989).

99. Moreno, M. S., Bolte, J., Klotz, J. & Melnick, D. Impact of megathrust geometry on inversion of coseismic slip from geodetic data: Application to the 1960 Chile earthquake. *Geophysical Research Letters* **36**, (2009).

100. Nagai, R., Kikuchi, M. & Yamanaka, Y. Comparative study on the source processes of recurrent large earthquakes in Sanriku-oki region : the 1968 Tokachi-oki earthquake and the 1994 Sanriku-oki earthquake. *Zisin* **54**, 267–280 (2001).

101. Yagi, Y. Source process of the Hyuga-nada earthquake of April 1, 1968 (M_< JMA> 7.5), and its relationship to the subsequent seismicity. *Zisin* **51**, 139–148 (1998).

102. Yagi, Y., Kikuchi, M., Yoshida, S. & Sagiya, T. Comparison of the coseismic rupture with the aftershock distribution in the Hyuga-nada Earthquakes of 1996. *Geophysical Research Letters* **26**, 3161–3164 (1999).

103. Yamanaka, Y. & Kikuchi, M. Asperity map along the subduction zone in northeastern Japan inferred from regional seismic data. *Journal of Geophysical Research: Solid Earth* **109**, (2004).

104. Tarantola, A. *Inverse Problem Theory and Methods for Model Parameter Estimation*. (Society for Industrial and Applied Mathematics, 2005). doi:10.1137/1.9780898717921.
105. Meade, B. J. Algorithms for the calculation of exact displacements, strains, and stresses for triangular dislocation elements in a uniform elastic half space. *Computers & Geosciences* **33**, 1064–1075 (2007).
106. van Rijsingen, E. M., Calais, E., Jolivet, R., Robertson, R. & Ryan, G. A. Inferring Interseismic Coupling Along the Lesser Antilles Arc: A Bayesian Approach. *Journal of Geophysical Research* 21 (2021).
107. DeMets, C., Gordon, R. G. & Argus, D. F. Geologically current plate motions. *Geophys J Int* **181**, 1–80 (2010).
108. Erickson, B. A. *et al.* The Community Code Verification Exercise for Simulating Sequences of Earthquakes and Aseismic Slip (SEAS). *Seismological Research Letters* **91**, 874–890 (2020).
109. Uphoff, C., May, D. A. & Gabriel, A.-A. A discontinuous Galerkin method for sequences of earthquakes and aseismic slip on multiple faults using unstructured curvilinear grids. *Geophysical Journal International* **233**, 586–626 (2023).
110. Biemiller, J., Gabriel, A. -A., May, D. A. & Staisch, L. Subduction Zone Geometry Modulates the Megathrust Earthquake Cycle: Magnitude, Recurrence, and Variability. *JGR Solid Earth* **129**, e2024JB029191 (2024).
111. Lapusta, N., Rice, J. R., Ben-Zion, Y. & Zheng, G. Elastodynamic analysis for slow tectonic loading with spontaneous rupture episodes on faults with rate- and state-dependent friction. *Journal of Geophysical Research: Solid Earth* **105**, 23765–23789 (2000).
112. Freedman, D. & Diaconis, P. On the histogram as a density estimator:L2 theory. *Z.*

710 *Wahrscheinlichkeitstheorie verw Gebiete* **57**, 453–476 (1981).

711

712

713

714

Supplementary Materials for

Do Coupled Megathrusts Rupture?

Bar Oryan* & Alice-Agnes Gabriel

*Corresponding author. Email: bar.oryan@columbia.edu

This PDF file includes:

Supplementary Text S1-S6
Figs. S1- S17
Table S4

Other Supplementary Materials (see table captions below):

Table S1
Table S2
Table S3

Text S1 - Choice of coupling models

Kamchatka

To the best of our knowledge, the only geodetic coupling model available for the section of the Kamchatka subduction zone along the Pacific–Eurasian plate interface—and one of the first kinematic coupling models ever established—is that of Bürgmann et al1. Bürgmann et al.1 used 12 permanent and 18 campaign GPS stations, operating over 4 and 3 years respectively, to estimate slip deficit rates across a range of smoothing values. Notably, Bürgmann et al[1]. do not report coupling values directly, but rather slip deficit rates along the megathrust. We here estimate coupling from their inference by normalizing the reported slip deficit rates by the maximum plate convergence rate of 8 $cm \cdot yr^{-1}$ and adopting a smoothing value of β=0.05, as in their preferred model.

Alaska

The subduction of the Pacific Plate beneath the North American Plate in southern Alaska has long been recognized as a source of large megathrust earthquakes, rendering the estimation of slip deficit and seismic potential a key research focus [2–4]. For our analysis, we rely on the coupling model compiled by Basset et al.[5], which synthesizes results from several studies, primarily based on GNSS observations, to quantify slip deficit along the Alaska margin. These sources include Elliott & Freymueller[3], who incorporated data from 84 continuous GNSS stations and 327 campaign sites, with most observations collected between 2002 and 2016. Additionally, Basset et al.[5] incorporated kinematic coupling estimates from Li & Freymueller[4], based on 78 campaign and continuous GPS stations spanning the period from 1992 to 2017.

Central America

Northern Mexico

Kinematic coupling along the northern Cocos plate beneath Mexico has been estimated by several studies over the past few decades [6–8] . Our here preferred model is that of Maubant et al.[7], who used recent geodetic observations, including GNSS and Sentinel-1 InSAR velocities collected over a 3.5-year period, to estimate coupling across the 3D megathrust geometry as constrained by Slab2. Out of the models we examined, this study reports the most spatially extensive coupling, spanning from western to eastern Mexico (106°W to 95°W), thereby enabling the inclusion of the largest number of earthquakes in our analysis. We note that their model occasionally reports negative coupling values, due to slow slip events in the region. In our analysis, we set those negative values to zero.

Costa Rica

A few estimates of interseismic coupling along the Cocos–Caribbean Plate interface in Costa Rica, primarily focused on the Nicoya Peninsula, have been published to date[9,10]. For our analysis, we rely on the model of Xue et al.[9], which incorporates the most up-to-date geodetic observations available at the time, including three years of L-band InSAR interferograms and GNSS velocity data from 19 continuous and 29 campaign GPS stations.

Sumatra

Surprisingly, despite Sumatra producing some of the largest megathrust earthquakes, we found only one study that provides coupling estimates spanning much of the island[11]. Chlieh et al.11 combines vertical displacement rates inferred from coral growth rings at 44 sites, spanning the period from 1962 to 2000, with horizontal GPS velocities from 33 sites surveyed during campaign-style observations between 1991 and 2001. The model also incorporates data from six continuous GPS stations deployed during the two years leading up to the 2004 Great Sumatra earthquake. For their inversion, Chlieh et al.11 simplified the megathrust interface to a planar dislocations dipping uniformly at 13°, beginning at the trench.

Colombia, Ecuador , and Peru

Colombia & Ecuador

The segment of the Nazca Plate that subducts beneath the South American Plate along the Ecuador–Colombia trench extends for approximately 900 km along-strike and has produced several large megathrust earthquakes. To the best of our knowledge, two estimates of interseismic coupling have been published for this region[12,13]. Our preferred model[13] incorporates the most up-to-date geodetic observations, relying on data from 113 GNSS sites distributed across Colombia, Panama, Ecuador, and Venezuela to compute coupling along the megathrust, constrained using the Slab2 geometry[14].

Peru

To our knowledge, two estimates of slip deficit rates have been published for the Central Andes subduction zone, where the Nazca Plate subducts beneath the South American Plate[15,16]. Here our preferred model, from Lovery et al.[15], relies on more recent geodetic observations, incorporating data from 47 permanent and 26 campaign GNSS sites collected between 1993 and 2022 to

estimate interseismic coupling along the megathrust from Lima to Arica. The model uses a 3D fault geometry derived from Slab2.0 and explores a range of smoothing parameters and reference frames. For our analysis, we adopt their preferred solution, computed in the Peruvian Sliver reference frame, using a 30 km smoothing constraint.

Chile

The Chilean margin is a well-studied region where numerous estimates of interseismic coupling along the subducting Nazca Plate have been published [17–22]. For our analysis, we use the model of Métois et al.[20] , which spans nearly the entire Chilean margin, extending over 3,000 km from 18°S to 38°S, and encompasses four earthquake slip models for events larger than Mw 8.0 (Fig. 1). The model incorporates 396 horizontal GNSS velocities along with 70 vertical slip rate estimates across the region, with some sites including data collected as early as the 1990s. To estimate slip deficit, the authors discretized the slab interface into a grid of 93 along-strike nodes (spaced every 0.25°) and 11 along-dip nodes, based on the Slab1 geometry, and solved for coupling at each node as well as for the Euler pole.

Coupling in Japan

Japan hosts three distinct subduction zones. In the southwest, the Nankai Trough marks the subduction of the Philippine Sea Plate beneath the Eurasian Plate. To the east, the Sagami Subduction Zone represents a relatively short (~350 km) segment where the Philippine Sea Plate subducts almost perpendicularly to the Nankai Trough. Further north, the Japan Trench marks the subduction of the Pacific Plate beneath the Eurasian Plate, extending through Tohoku and into Hokkaido.

Interseismic coupling along these three subduction zones has been estimated by several groups, typically focusing on individual segments[23–29]. For our analysis, we adopt the model of Loveless & Meade (2015), for the Japan trench. Loveless & Meade simultaneously estimated slip deficit across all three subduction zones using a 3D elastic block-model consisting of 20 tectonic blocks and relying on approximately 19 years of GNSS observations from ~800 sites. Their model extends all the way to Hokkaido allowing us to include a number of megathrust earthquakes that would not align with other coupling maps (Fig. 1). We note that Loveless & Meade reported two coupling models, one in which the plate interface near the trench is locked, and another where it is freely slipping. We use the model in which the trench is locked, consistent with interpretations that high apparent coupling near the trench results from stress shadow effects [24,30]. For Sagami we rely on coupling inversions that employed 840 landbase GNSS sites as well as 23 campaign

style acoustic offshore geodetic measurements [27]. For the Nankai section, we rely on a study that used the same dataset as Sagami but applied a Markov Chain algorithm to probe the posterior distribution, together with Green's functions based on realistic Earth properties and structures, to obtain coupling fields with minimal assumptions[28].

Himalayas

Numerous studies have sought to characterize interseismic coupling along the Himalayan plate boundary, where the Indian Plate converges with the Eurasian Plate along the Main Himalayan Thrust[31–37]. Our preferred model[36] incorporates the most up-to-date geodetic observations and estimates coupling across the entire margin, from 74°E to 92°E. Panda & Lindsey (2024) analyzed data from 839 GNSS sites spanning the Indian Plate, the Tibetan Plateau, and the Indo-Burmese Arc. They tested over 200 block model configurations in an iterative framework, systematically accounting for block motions and internal strain to isolate the coupling signal along the Main Himalayan Thrust. Their three best-fitting models consistently indicate that the megathrust is largely locked. For our analysis, we adopt their preferred solution, based on the block geometry that provides the best fit to the observed data.

Kinematic coupling models not used

We would like to note a few additional coupling studies that we obtained but did not use, as we did not find records of finite slip models that ruptured these segments.

Southern Mexico, Guatemala, El Salvador, and Nicaragua

Along the Cocos–Caribbean Plate interface, coupling has not been studied in detail, and we identified only one study38 that provides a quantitative estimate for its northern section. Ellis et al.[38] used data from over 200 GNSS stations to model the elastic and kinematic behavior of southern Mexico, Guatemala, El Salvador, and Nicaragua, resolving motion across eight tectonic plates and blocks using the TDEFNODE software. For our analysis, we use the coupling they estimated for the Cocos–forearc sliver, spanning from southern Mexico to Nicaragua.

Java

Two estimates of slip rate have been proposed for the western and eastern segments of the Sunda subduction zone in Java. The first is based on three years of data from 13 GNSS stations collected between 2008 and late 2010 and was used to estimate coupling in western Java[39]. The second incorporates data from 37 GNSS stations distributed across central and eastern Java,

spanning the period from 2008 to 2014[40]. Notably, neither study reports coupling values directly; instead, they provide slip rate estimates, which we normalize by the maximum slip rate to approximate coupling. We also note that the resulting coupling distributions do not align with observed finite slip models and are therefore not included in our primary analysis. Nonetheless, we present these models here and in Fig. 1 for completeness.

Text S2 - Sensitivity of slip–coupling correlation to choice of κ

To test the sensitivity of our results to the choice of κ, we compute the CDFs for all megathrust events using 13 different κ values ranging from 21 to 10^5 km^{-3}. For κ=3500 km^{-3} and κ=750 km^{-3}, the maximum differences are less than 1% and 5%, respectively (Fig. S2). We therefore adopt κ = 3500 km^{-3} for our primary analysis and 750 km^{-3} for the null model and spatial uncertainty tests.

We further examine the convergence of the PDF and CDF (Fig. S3) using the Tocopilla megathrust earthquake [41] (Fig. 2). The CDF stabilizes with just over 10,000 samples, whereas the PDF fails to converge even with one million samples, due in part to the clustering of samples near the edges of the distribution.

Text S3 - Sensitivity of slip–coupling correlation to finite-fault models

Variations in inversion methods and input data, including geodetic, seismic, and tsunami observations, can produce different spatial coseismic slip distributions[42]. To evaluate how such differences affect the slip–coupling correlation, we analyze eleven additional published finite-slip models for the 2011 Tōhoku, Japan, earthquake (Fig. S5 and Table S2)[43–53] and additional four for the 2010 Maule, Chile, earthquake[54–57] (Fig. S6 and Table S3) , computing the slip–coupling CDF for each (Fig S7). We note that except for one outlier for the Maule event, slip-coupling correlation shows comparable patterns.

Text S4 - Sensitivity of slip–coupling correlation to smoothing constraints

Kinematic coupling models often apply spatial smoothing to slip deficit estimates, which can blur sharp contrasts and create variations in coupling patterns. To assess the impact of smoothing (Fig. S8), we compare slip–coupling CDFs (Fig. S9) derived from three smoothing levels in Peru[15] and four in Kamchatka[1] , where coupling maps are reported for each case. The correlations we observe, particularly in Kamchatka, demonstrate that the choice of smoothing can introduce variance in slip–coupling relationships, even though the overall pattern remains consistent.

Text S5 - Sensitivity of slip–coupling correlation to choice of coupling model

We test the slip–coupling correlation for five subduction zones [6,7,9,10,28,28,32,36,58,59] where additional coupling models are available beyond our preferred model (Fig. S10). To ensure consistency, we include only megathrust earthquakes whose rupture areas span the

full extent of all available coupling models. Across these cases, we find broadly similar patterns among the different coupling models, with the main exception of Nankai, where the Nishimura [27] model shows greater divergence from the others.

Text S6 - Sensitivity of slip–coupling correlation to choice of coupling model

We estimate the confidence that the observed slip–coupling distribution exceeds the null for each of the 61 megathrust earthquakes by running 1,000 bootstrap experiments. In each experiment we resample both ensembles with replacement, drawing as many curves as there are in each set (500), so individual CDFs may appear multiple times while others may not be selected. For every experiment we compute the difference between the observed and null CDFs (eq. 7) and record whether it is positive. Confidence at a given coupling is defined as the fraction of experiments with a positive difference. For example, a value of 0.95 means that in 950 out of 1,000 experiments the difference is positive, which we interpret as strong evidence that the observed distribution exceeds the null. We repeat this procedure for every earthquake (Fig. S12) and report confidence as a function of coupling. The results mirror those in the main text: smaller earthquakes show more variable slip–coupling relationships and rarely sample the highest coupling values, whereas larger events ($Mw \geq 7.5$) consistently concentrate slip in strongly coupled regions.

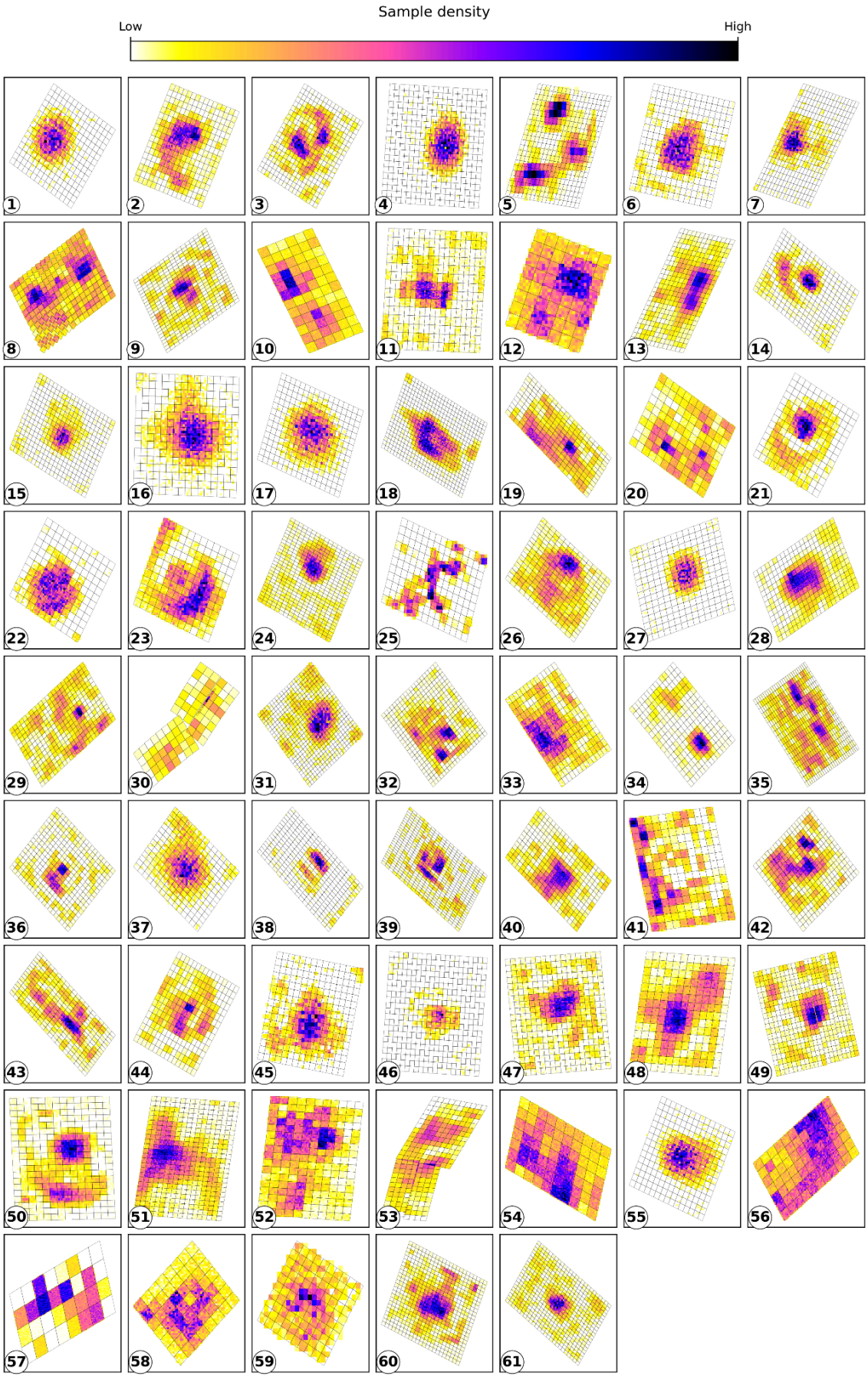
Sample density
Low
High
1
2
3
4
5
6
7
8
9
10
11
12
13
14
15
16
17
18
19
20
21
22
23
24
25
26
27
28
29
30
31
32
33
34
35
36
37
38
39
40
41
42
43
44
45
46
47
48
49
50
51
52
53
54
55
56
57
58
59
60
61

Fig. S1 – Sixty one finite slip models and their discretization. Black lines indicate the positions of subfaults comprising each model. The colormap shows the density of samples across the fault surface, with total sample counts for each model provided in Table S1. Event properties are listed in Table S1.

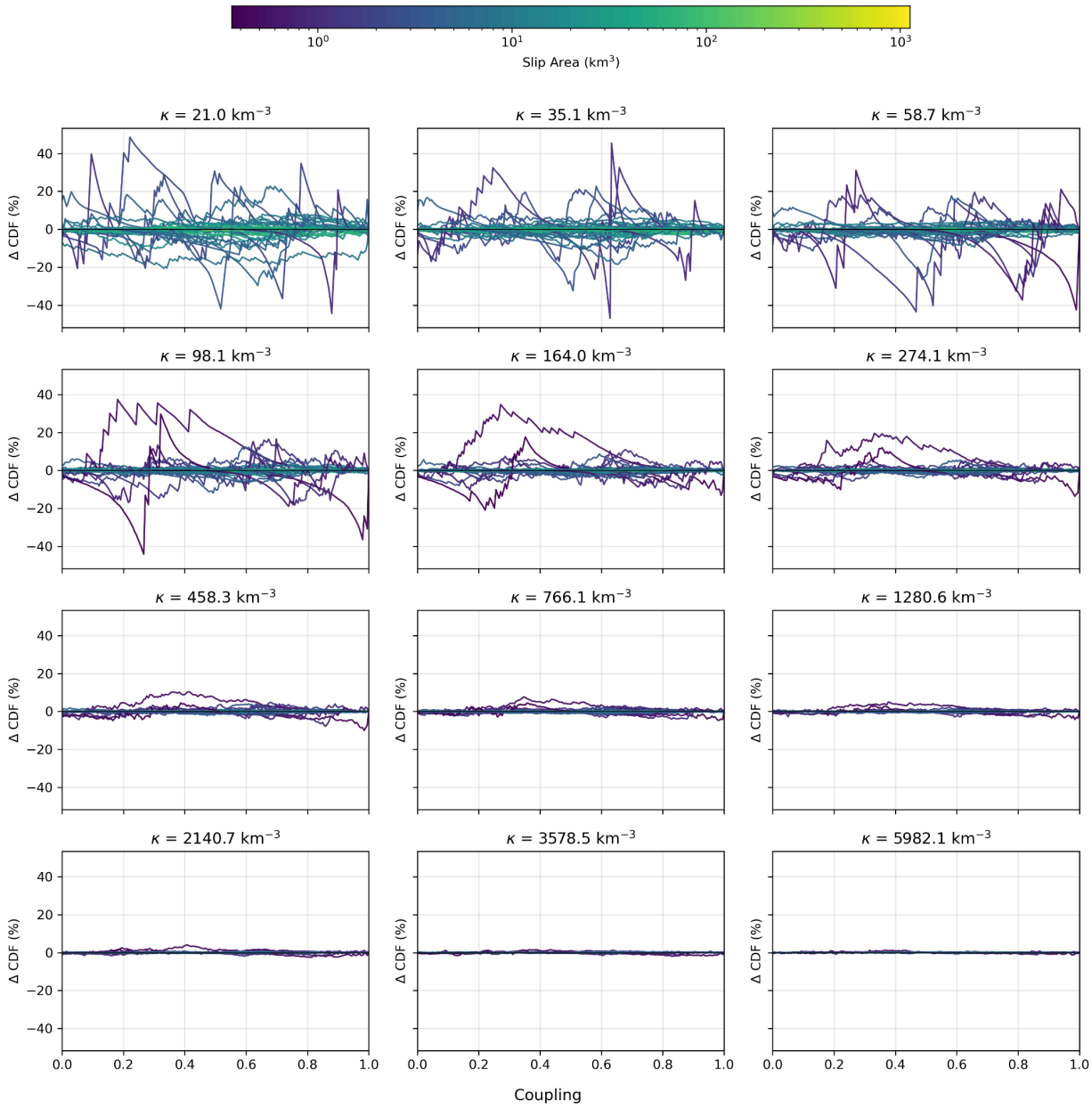

Fig. S2 – Slip–coupling difference CDFs for varying κ. Each panel shows the difference between CDFs for 61 megathrust events at a given κ, computed relative to the CDF estimated using $\kappa = 10^5$ km^{-3}. Curves are color-coded by the total slip area of each megathrust.

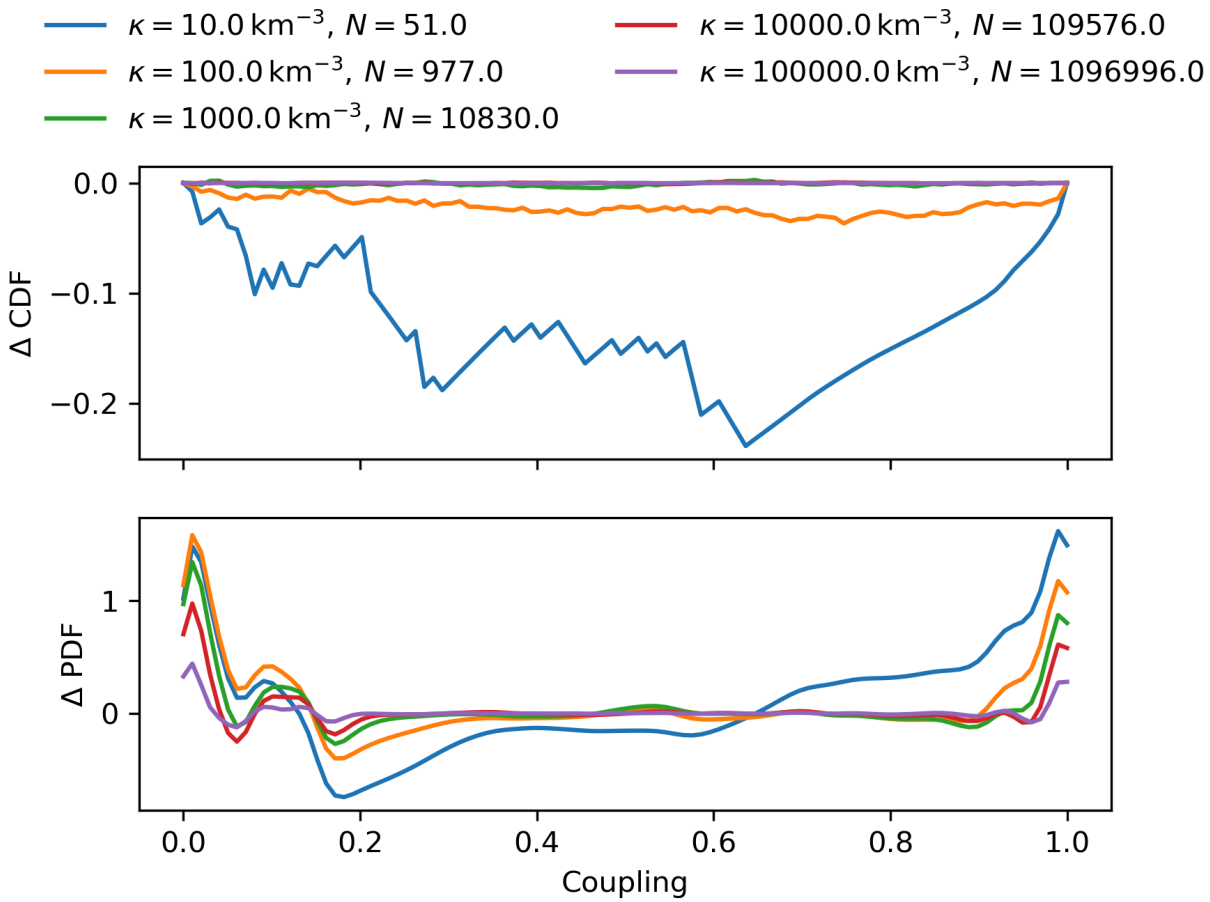

Fig. S3 – Slip–coupling difference CDFs and PDFs for varying κ. Panels show the difference between CDFs and PDFs for the 2017 Mw 7.7 Tocopilla megathrust earthquake [41] at a given κ, computed relative to those estimated using $\kappa = 5 \cdot 10^6$ km^{-3}.

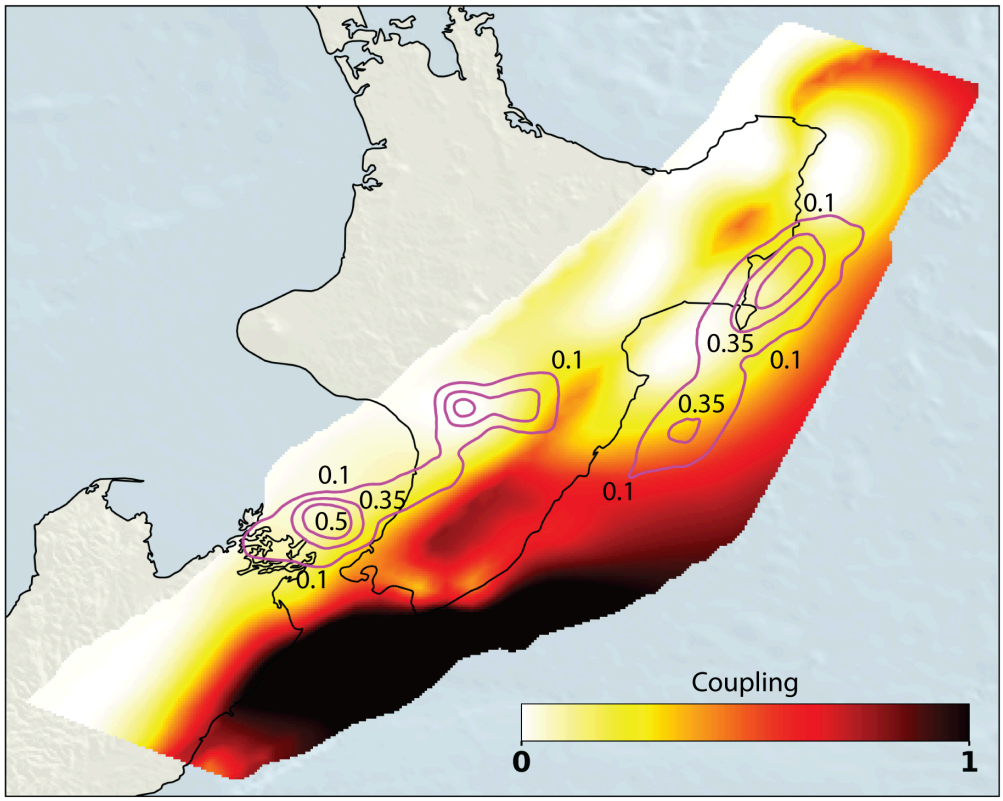

Fig. S4 – Accumulated slow slip and coupling for the Hikurangi margin. Magenta contours show three intervals of accumulated slow slip (0.1,0.35 and 0.5 meters) between 2002-2014 in New Zealand's Northern Island[60]. Coupling is determined from GNSS data recorded between 2006-2016[61]. We use these to compute the slow-slip-coupling correlation.

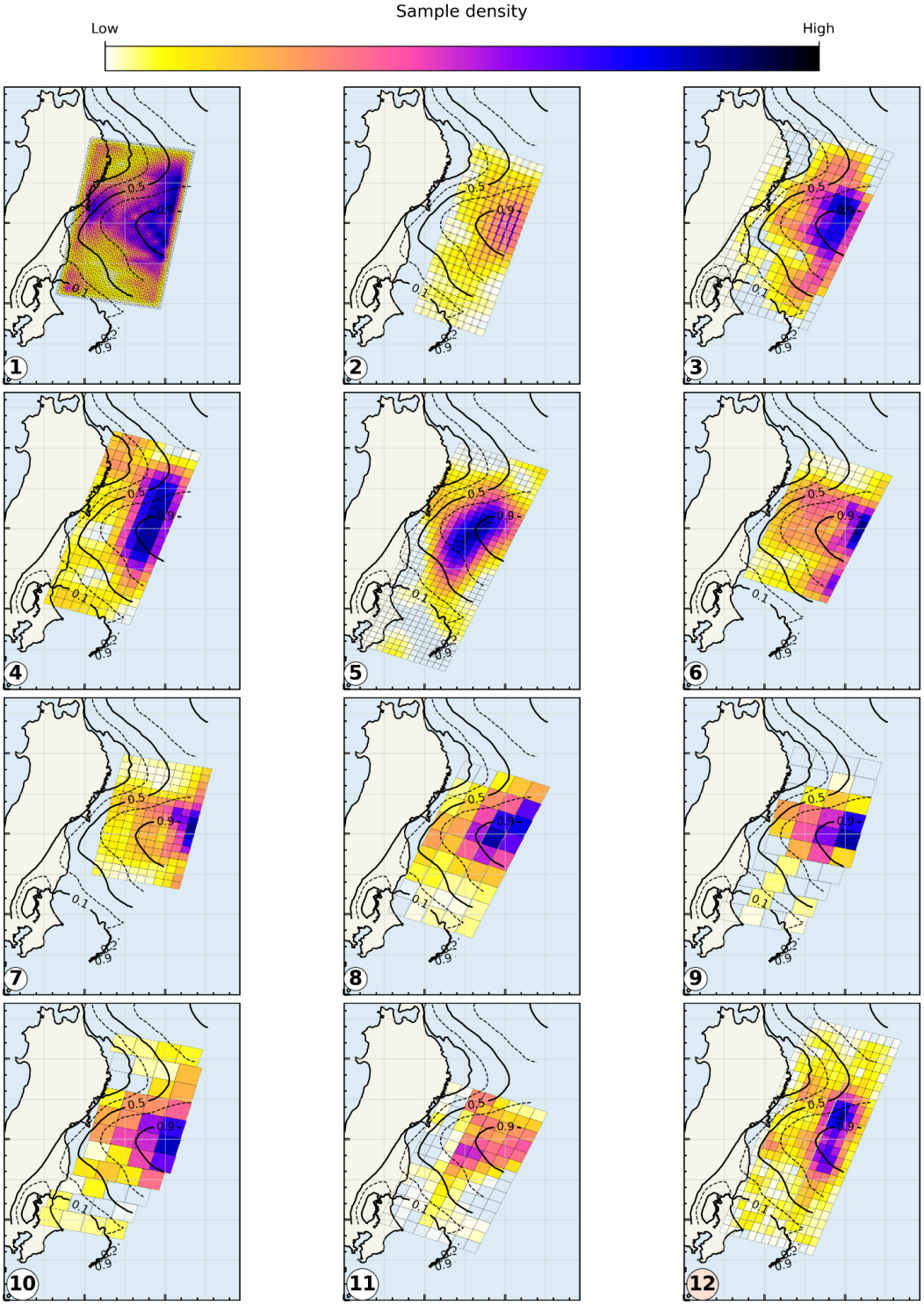

Fig. S5 – Twelve Tōhoku finite slip models [43–53]**.** Black lines indicate the positions of subfaults comprising each model. The colormap shows the density of samples across the fault surface,

with total sample counts for each model provided in Table S2. Black contours mark coupling values. Event properties are also listed in Table S2; event 12 corresponds to the model used in the main text[41].

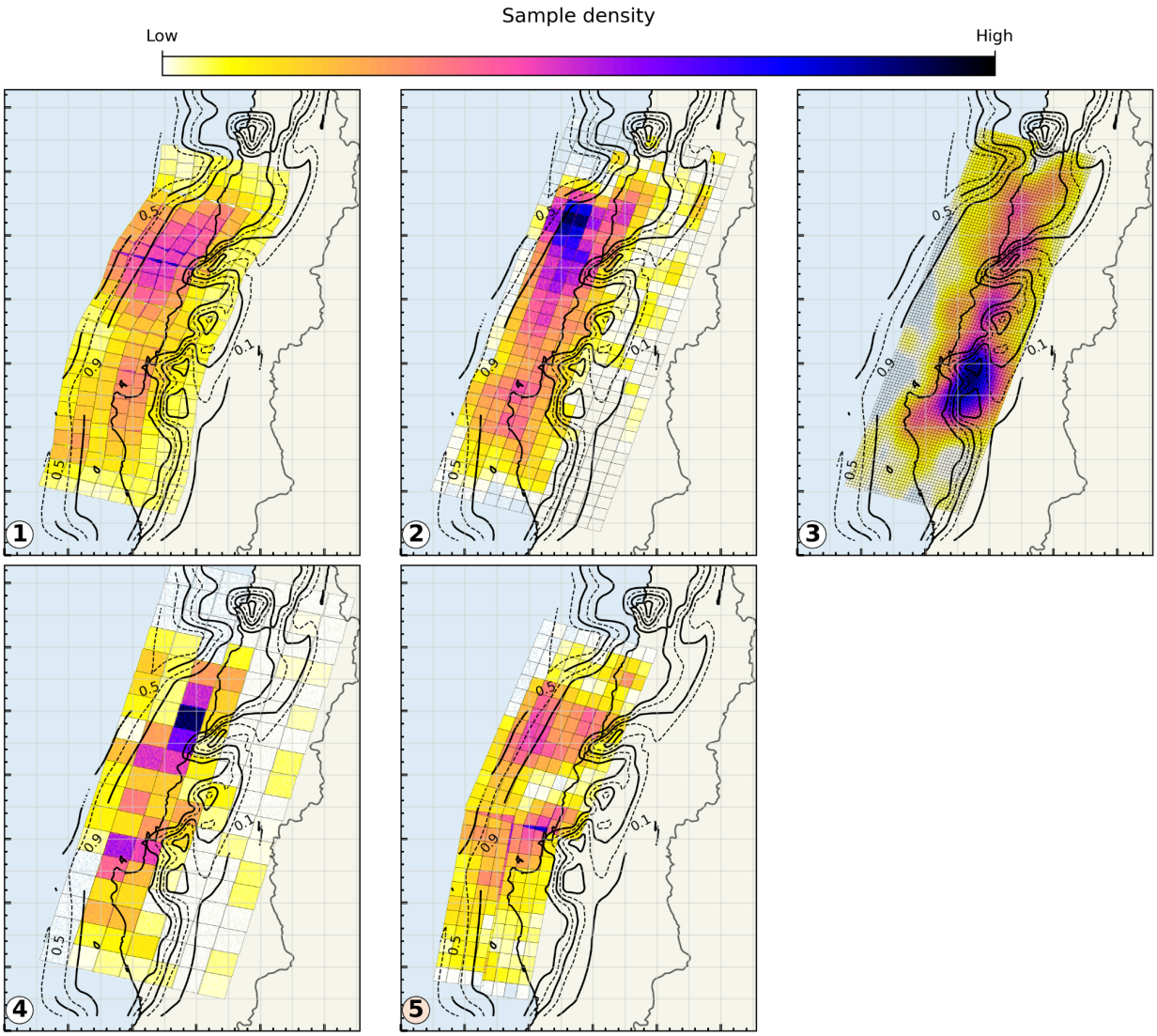

Fig. S6 – Five Maule finite slip models [54–57] and their discretization. Black lines indicate the positions of subfaults comprising each model. The colormap shows the density of samples across the fault surface, with total sample counts for each model provided in Table S2. Black contours mark coupling values. Event properties are also listed in Table S2; event 5 corresponds to the model used in the main text[41].

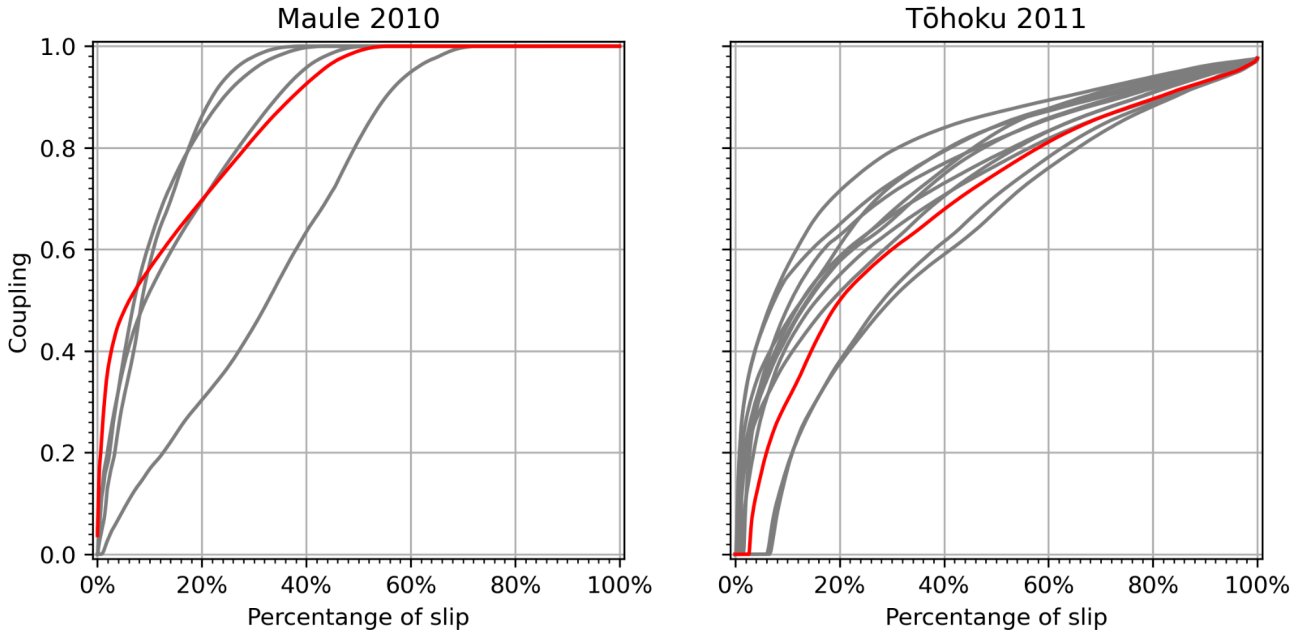

Fig. S7 – Slip-Coupling correlations for different finite slip models for the Maule and Tohoku megathrust earthquakes. Red and grey lines indicate finite slip models we used in the main text[41] and additional models[43–57] we examine (Text S3), respectively.

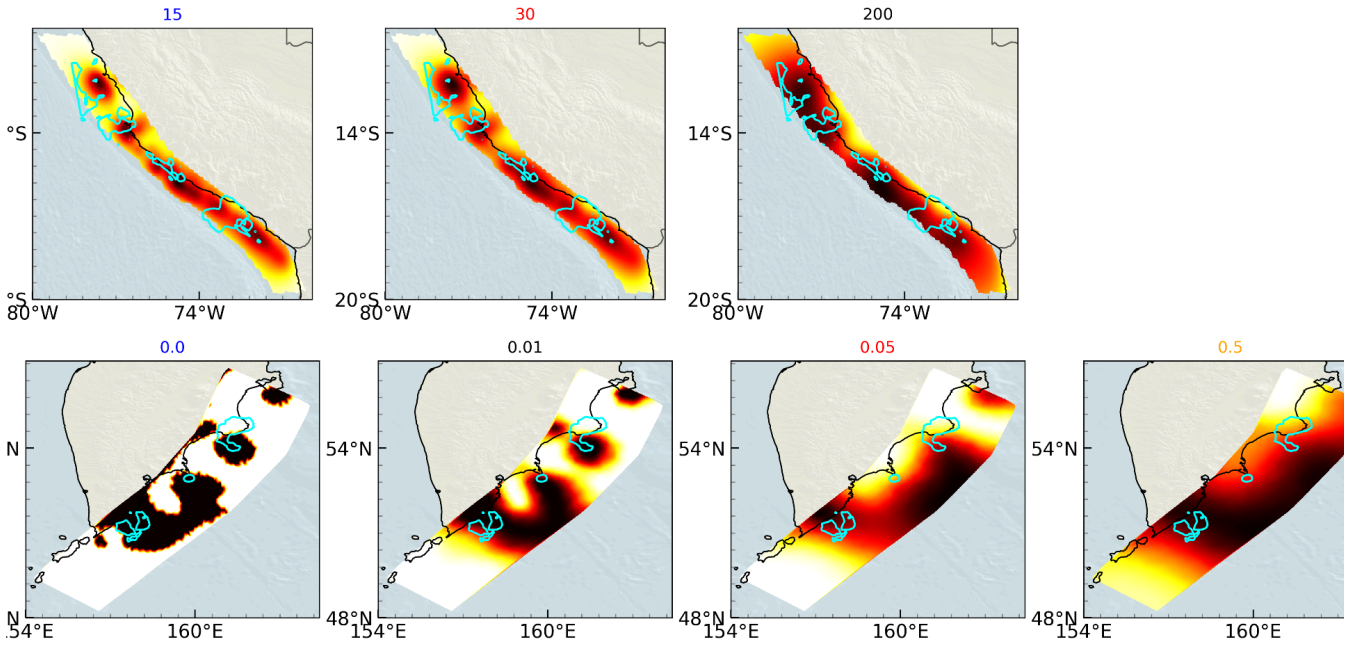

Fig. S8 – Peru[15] and Kamchatka[1] kinematic coupling distributions for varying smoothing constraints. Cyan contours represent slip contours for regions where at least 30% of the maximum slip has been accumulated. Red Smoothing factors denote the preferred model used in the main text, corresponding to the authors' favored solution. Other colors correspond to slip–coupling correlations shown in Fig. S9.

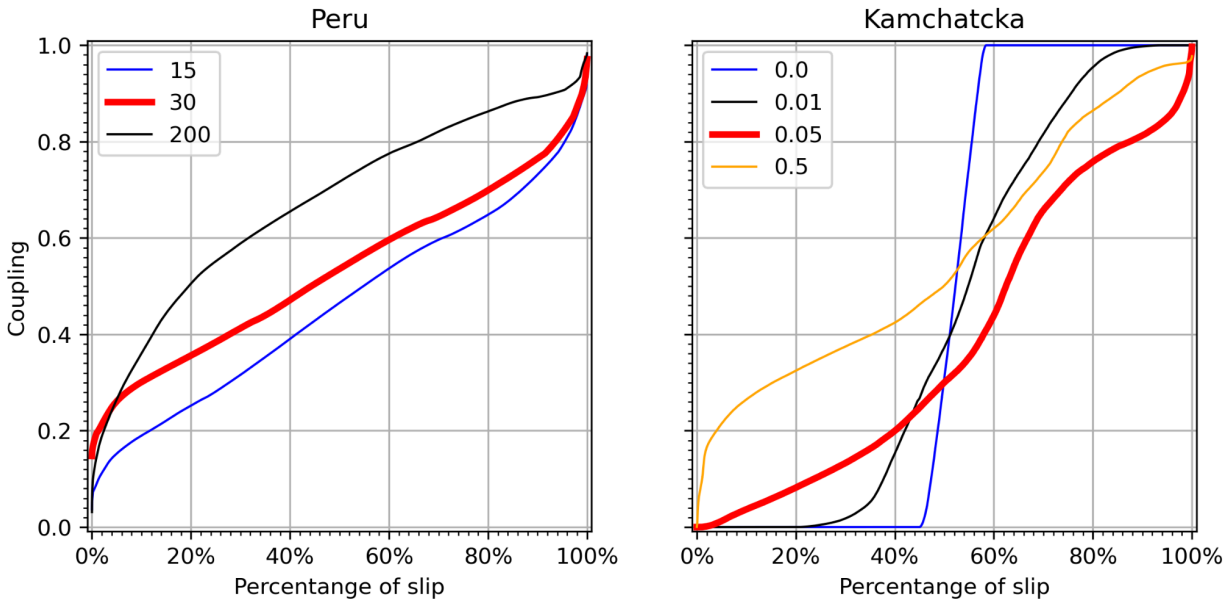

Fig. S9 – Slip-coupling CDF for varying smoothing factors in Peru [15] and Kamchatka [1]. Smoothing factors marked in red indicate models used in the main text.

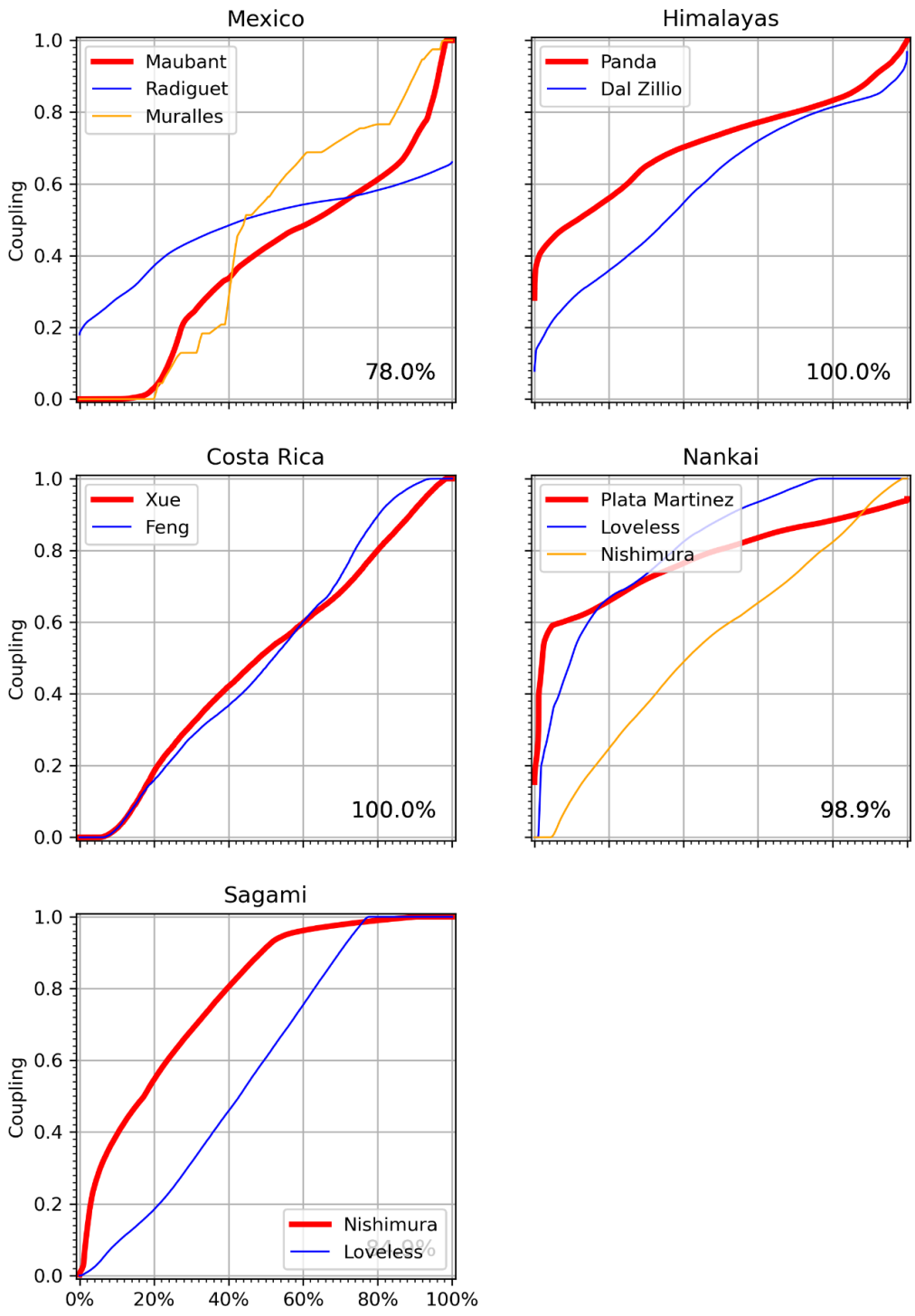
Mexico
Maubant
Radiguet
Muralles
78.0%
Himalayas
Panda
Dal Zillio
100.0%
Costa Rica
Xue
Feng
100.0%
Nankai
Plata Martinez
Loveless
Nishimura
98.9%
Sagami
Nishimura
Loveless
Coupling
0.0
0.2
0.4
0.6
0.8
1.0
0%
20%
40%
60%
80%
100%
Percentange of slip

Fig. S10 – Slip–coupling CDFs for different coupling models[6,7,9,10,28,28,32,36,58,59]**.** Coupling models marked in red indicate models used in the main text. The ratio of sample points used in this analysis to those used in the main text is shown in the lower right corner.

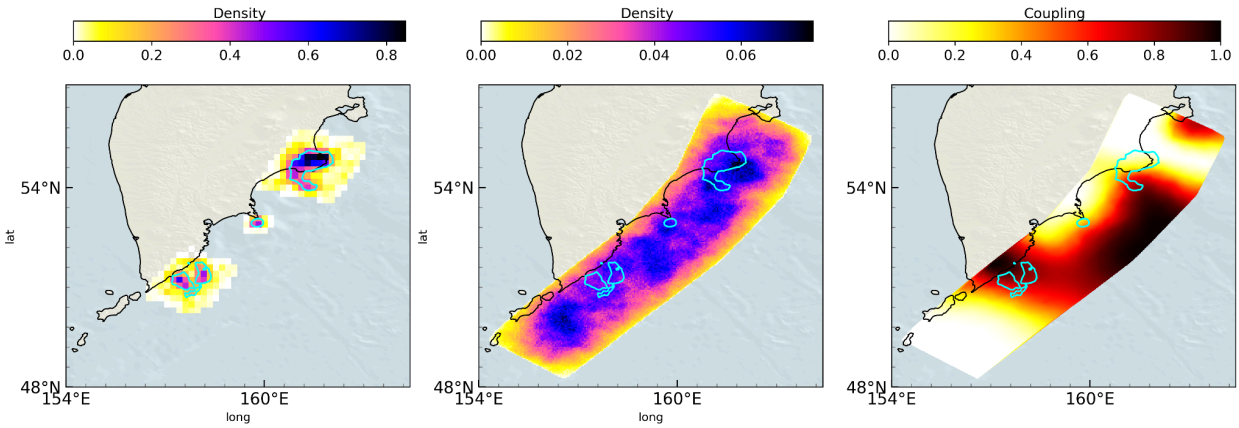

Fig S11 - Comparison between observed and synthetic (null) megathrust earthquake models in Kamchatka**.** A - Density of slip samples for three observed megathrusts. B - Density of slip samples from 1,500 synthetic realizations of the same megathrusts. C - Our preferred coupling model for Kamchatka [1]. Cyan contours delineate regions where slip exceeded 30% of the maximum megathrust slip.

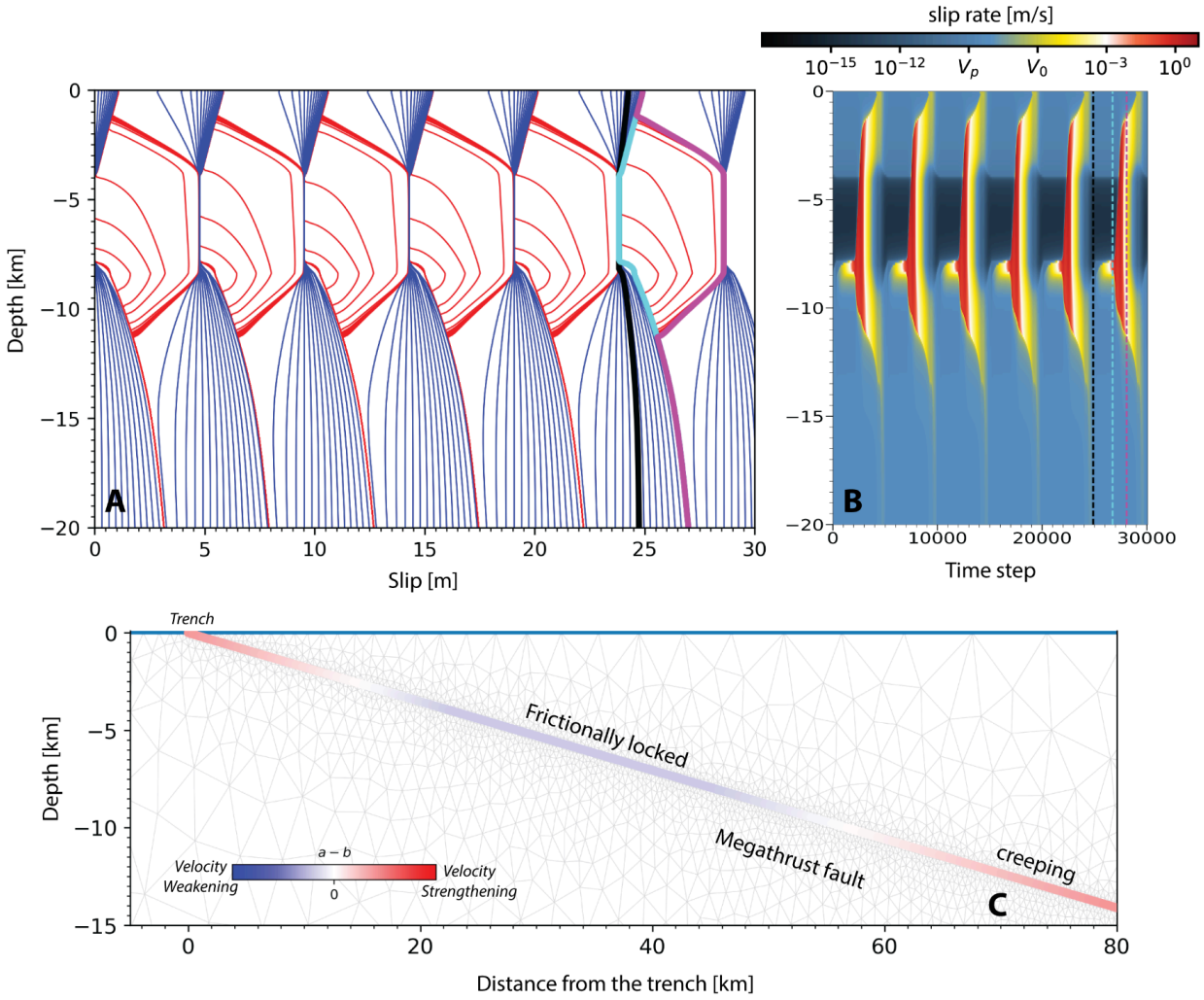

Fig. S12 - Numerical simulations of seismic and aseismic slip along an idealized 2D subduction zone over 1000 years (after the spin-up phase) using the volumetric code tandem [62]. A - Slip contours on the megathrust, plotted every 10 seconds during coseismic rupture (red) and every 5 years during the interseismic period (blue). B - Slip rate along the megathrust. Black and cyan curves denote the 40-year interseismic period used to compute coupling (Eq. 10). Cyan and magenta mark the coseismic interval.C - Finite-element mesh used for the seismic cycle simulations. Grey lines show triangular elements, and the megathrust fault is color-coded by frictional properties guided by geodetic observations and prior simulations of Cascadia [24,63,64]. See table S4 for complete descriptions of model parameters.

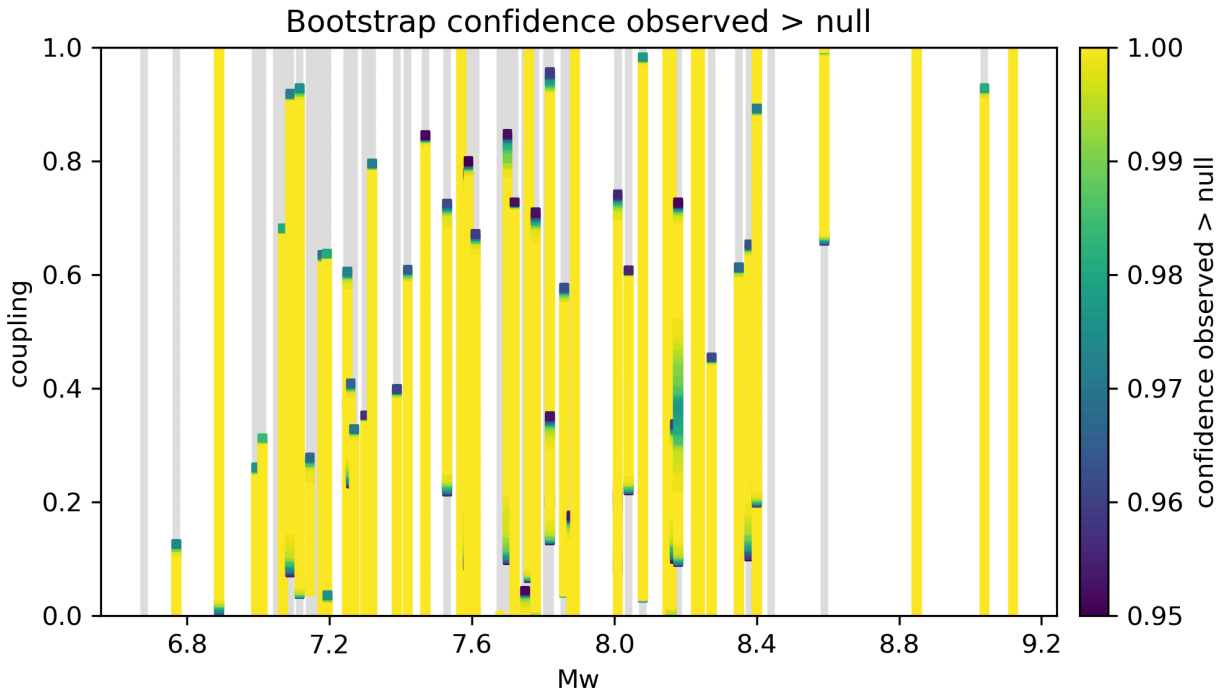

Figure S13. Bootstrap confidence that observed slip–coupling distributions exceed the null. Vertical stripes show, for each megathrust earthquake, the confidence that observed slip is greater than the null at a given coupling value. Grey shading marks confidence levels below 95%, indicating that a reliable correlation cannot be established.

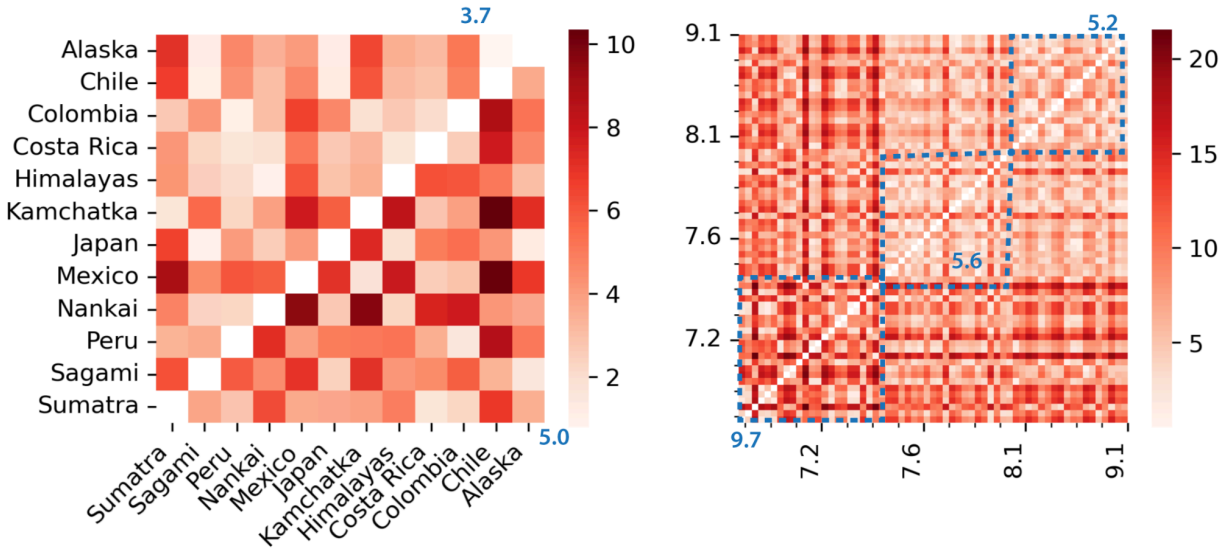

Fig S14 – Slip–coupling similarities across individual earthquakes and subduction margins. Left - Pairwise L2 distances among the 12 margins; blue numbers give mean distances for both null-corrected and uncorrected cases. Right - Pairwise L2 distances among the 61 megathrust earthquakes; blue numbers denote mean within-box values.

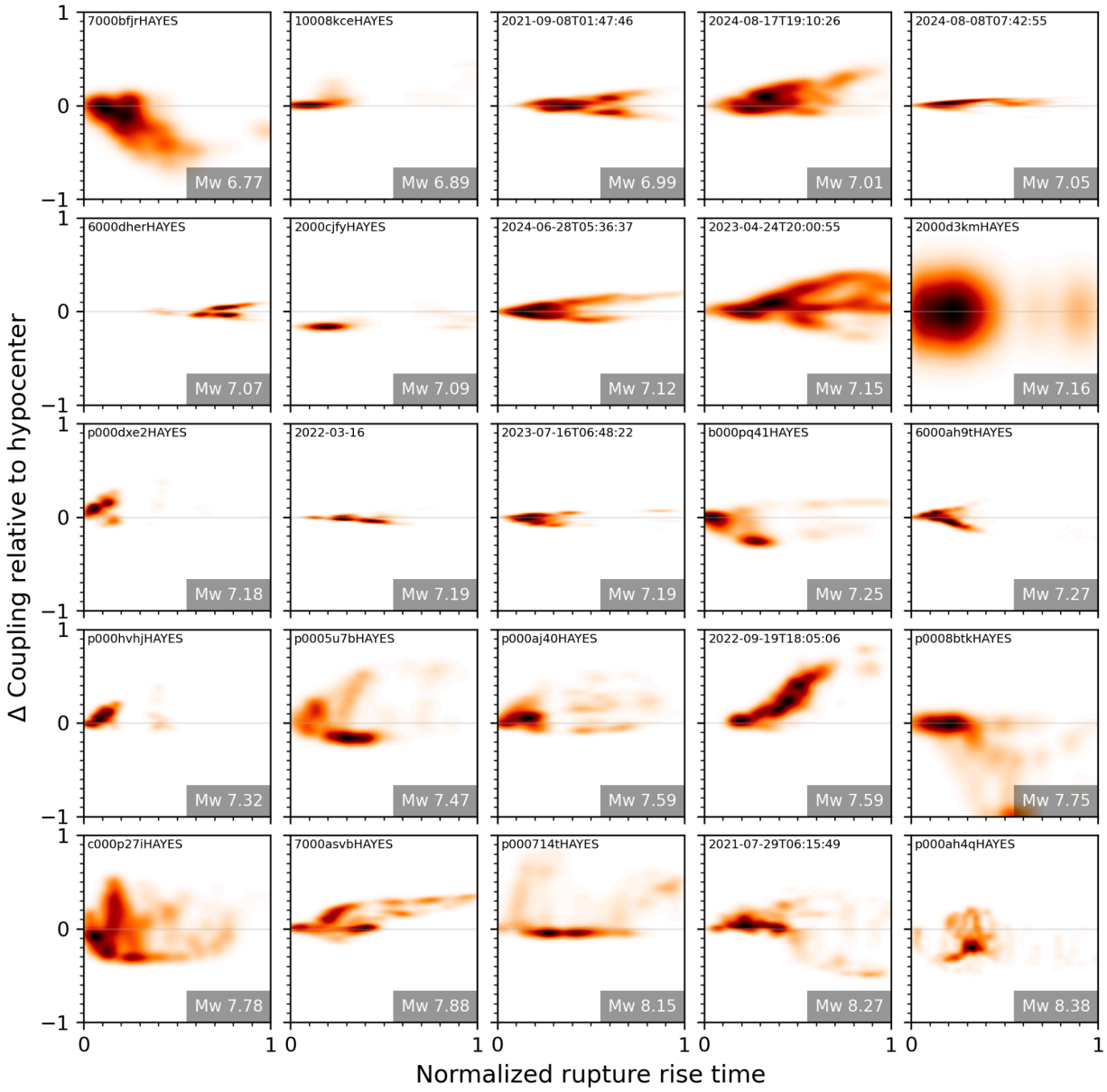

Fig S15 – Spatiotemporal patterns of slip for 25 megathrust. Colormap shows Probability density of normalized rupture rise time and coupling relative to the hypocenter for each of the 25 megathrust earthquakes. The upper left corner shows the unique identifier of each event (Table S1).

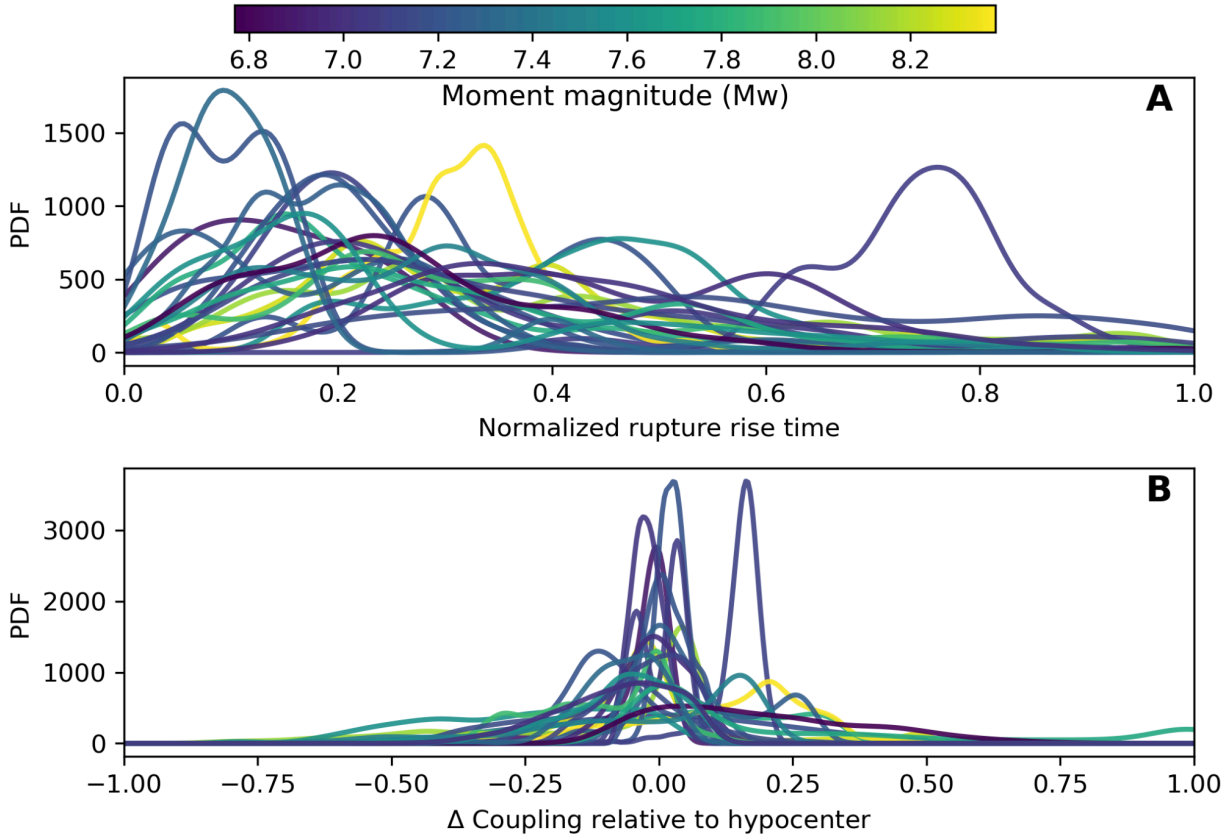

Figure S16 – Spatiotemporal patterns of slip for 25 megathrust earthquakes. Panels show PDFs of coupling relative to the hypocenter and normalized rise time for each event, color-coded by moment magnitude.

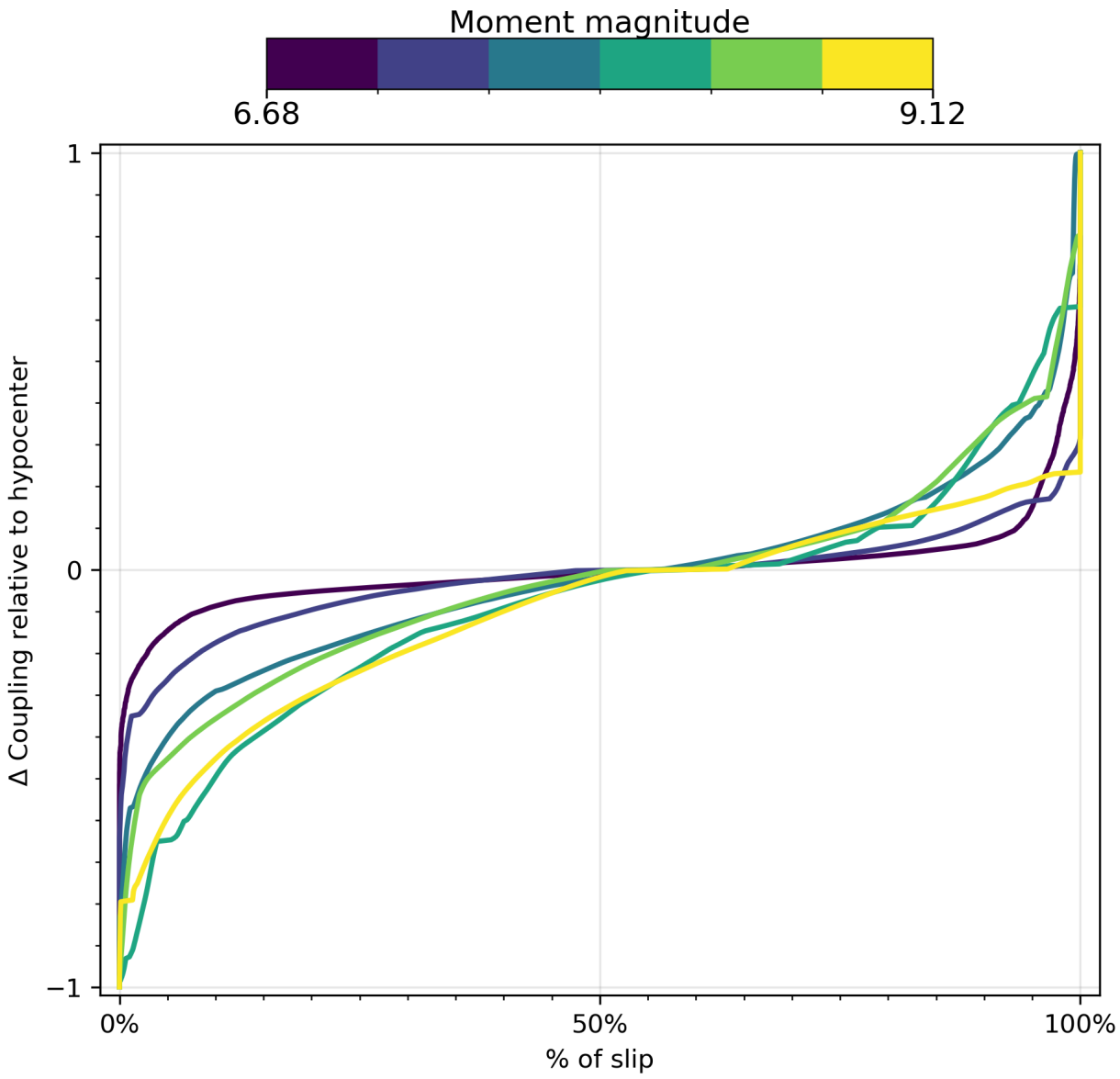

Figure S17 – CDFs of coupling relative to the hypocenter for 61 megathrust earthquakes binned into 6 groups based on moment magnitude. Slip is concentrated almost equally above coupling values above and below the initial hypocenter and does not show a strong preference across magnitudes.

Table S1 - Location, date, and type and number of observations used to constrain all finite fault models used in our main text analysis. BODY refers to body-wave arrivals; GNSS to static or campaign Global Navigation Satellite System; SGM refers to strong ground motion records from accelerometers; SURF represents surface-wave observations; TELE corresponds to teleseismic broadband waveforms; TRIL indicates horizontal trilateration surveys based on distance measurements; Level refers to leveling surveys measuring vertical displacements; TIDE refers to tide-gauge records from tsunami waveforms; and Other includes miscellaneous sources not classified elsewhere. A value of 999 indicates that the data type was used in the inversion, but the number of observations is not reported. Total slip area is noted in km^3.

Table S2 - Type of observations used to constrain eleven finite fault models for the Tohoku March 11, 2011, megathrust event in Japan. See Table S1 for a full description.

Table S3 - Types of observations used to constrain four finite fault models of the February 27, 2010 Mw 8.8 Maule megathrust earthquake in Chile. See Table S1 for a full description.

Parameter	Symbol	Unit	Value
Critical distance	D_{RS}	m	0.01
Reference slip rate	V_0	m/s	1e-6
Reference friction coefficient	f_0	–	0.6
Shear modulus	μ	GPa	30
Lamé parameter	λ	GPa	30
Half the shear-wave impedance for radiation damping	η	MPa·s/m	4.62
Initial normal stress	σ□	MPa	50
Rate-and-state evolution effect parameter	b	–	0.015
Convergence rate	V□	cm/yr	3.1

Table S4 - Model parameters used in the numerical simulations.

References

1. Bürgmann, R. *et al.* Interseismic coupling and asperity distribution along the Kamchatka subduction zone. *Journal of Geophysical Research: Solid Earth* **110**, (2005).

2. Drooff, C. & Freymueller, J. T. New Constraints on Slip Deficit on the Aleutian Megathrust and Inflation at Mt. Veniaminof, Alaska From Repeat GPS Measurements. *Geophysical Research Letters* **48**, e2020GL091787 (2021).

3. Elliott, J. & Freymueller, J. T. A Block Model of Present-Day Kinematics of Alaska and Western Canada. *Journal of Geophysical Research: Solid Earth* **125**, e2019JB018378 (2020).

4. Li, S. & Freymueller, J. T. Spatial Variation of Slip Behavior Beneath the Alaska Peninsula Along Alaska-Aleutian Subduction Zone. *Geophysical Research Letters* **45**, 3453–3460 (2018).

5. Bassett, D., Shillington, D. J., Wallace, L. M. & Elliott, J. L. Variation in slip behaviour along megathrusts controlled by multiple physical properties. *Nat. Geosci.* **18**, 20–31 (2025).

6. Cosenza-Muralles, B. *et al.* GPS-derived interseismic fault locking along the Jalisco–Colima segment of the Mexico subduction zone. *Geophysical Journal International* **228**, 2174–2197 (2022).

7. Maubant, L. *et al.* Interseismic coupling along the Mexican subduction zone seen by InSAR and GNSS. *Earth and Planetary Science Letters* **586**, 117534 (2022).

8. Radiguet, M. *et al.* Triggering of the 2014 Mw7.3 Papanoa earthquake by a slow slip event in Guerrero, Mexico. *Nature Geosci* **9**, 829–833 (2016).

9. Xue, L., Schwartz, S., Liu, Z. & Feng, L. Interseismic megathrust coupling beneath the Nicoya Peninsula, Costa Rica, from the joint inversion of InSAR and GPS data. *Journal of Geophysical Research: Solid Earth* **120**, 3707–3722 (2015).

10. Feng, L. *et al.* Active deformation near the Nicoya Peninsula, northwestern Costa Rica, between 1996 and 2010: Interseismic megathrust coupling. *Journal of Geophysical Research: Solid Earth* **117**, (2012).

11. Chlieh, M., Avouac, J. P., Sieh, K., Natawidjaja, D. H. & Galetzka, J. Heterogeneous coupling of the Sumatran megathrust constrained by geodetic and paleogeodetic measurements. *Journal of Geophysical Research: Solid Earth* **113**, (2008).

12. Chlieh, M. *et al.* Distribution of discrete seismic asperities and aseismic slip along the Ecuadorian megathrust. *Earth and Planetary Science Letters* **400**, 292–301 (2014).

13. Chlieh, M. *et al.* Seismic and Aseismic Cycle of the Ecuador–Colombia Subduction Zone. *Front. Earth Sci.* **9**, (2021).

14. Hayes, G. P. *et al.* Slab2, a comprehensive subduction zone geometry model. *Science* **362**, 58–61 (2018).

15. Lovery, B. *et al.* Heterogeneous Locking and Earthquake Potential on the South Peru Megathrust From Dense GNSS Network. *Journal of Geophysical Research: Solid Earth* **129**, e2023JB027114 (2024).

16. Perfettini, H. *et al.* Seismic and aseismic slip on the Central Peru megathrust. *Nature* **465**, 78–81 (2010).

17. Drápela, J., Calisto, I. & Moreno, M. Locking-derived tsunami scenarios for the most recent megathrust earthquakes in Chile: implications for tsunami hazard assessment. *Nat Hazards* **107**, 35–52 (2021).

18. Li, S., Moreno, M., Bedford, J., Rosenau, M. & Oncken, O. Revisiting viscoelastic effects on interseismic deformation and locking degree: A case study of the Peru-North Chile subduction zone. *Journal of Geophysical Research: Solid Earth* **120**, 4522–4538 (2015).

19. Métois, M., Socquet, A. & Vigny, C. Interseismic coupling, segmentation and mechanical behavior of the central Chile subduction zone. *Journal of Geophysical Research: Solid Earth* **117**, (2012).

20. Métois, M., Vigny, C. & Socquet, A. Interseismic Coupling, Megathrust Earthquakes and Seismic Swarms Along the Chilean Subduction Zone (38°–18°S). *Pure Appl. Geophys.* **173**, 1431–1449 (2016).

21. Moreno, M. *et al.* Heterogeneous plate locking in the South–Central Chile subduction zone: Building up the next great earthquake. *Earth and Planetary Science Letters* **305**, 413–424 (2011).

22. Moreno, M. *et al.* Heterogeneous plate locking in the South–Central Chile subduction zone: Building up the next great earthquake. *Earth and Planetary Science Letters* **305**, 413–424 (2011).

23. Abe, D. & Yoshioka, S. Spatiotemporal distributions of interplate coupling in Tohoku, northeast Japan, for 14 years prior to the 2011 Tohoku-oki earthquake inverted from GNSS data. *Tectonophysics* **838**, 229479 (2022).

24. Lindsey, E. O. *et al.* Slip rate deficit and earthquake potential on shallow megathrusts. *Nat. Geosci.* **14**, 321–326 (2021).

25. Loveless, J. P. & Meade, B. J. Kinematic Barrier Constraints on the Magnitudes of Additional Great Earthquakes Off the East Coast of Japan. *Seismological Research Letters* **86**, 202–209 (2015).

26. Loveless, J. P. & Meade, B. J. Geodetic imaging of plate motions, slip rates, and partitioning of deformation in Japan. *Journal of Geophysical Research: Solid Earth* **115**, (2010).

27. Nishimura, T., Yokota, Y., Tadokoro, K. & Ochi, T. Strain partitioning and interplate coupling along the northern margin of the Philippine Sea plate, estimated from Global Navigation Satellite System and Global Positioning System-Acoustic data. *Geosphere* **14**, 535–551 (2018).

28. Plata-Martinez, R. *et al.* Revisiting Slip Deficit Rates and Its Insights Into Large and Slow Earthquakes at the Nankai Subduction Zone. *Journal of Geophysical Research: Solid Earth* **129**, e2023JB027942 (2024).

29. Suwa, Y., Miura, S., Hasegawa, A., Sato, T. & Tachibana, K. Interplate coupling beneath NE Japan inferred from three-dimensional displacement field. *Journal of Geophysical Research: Solid Earth* **111**, (2006).

30. Almeida, R. *et al.* Can the Updip Limit of Frictional Locking on Megathrusts Be Detected Geodetically? Quantifying the Effect of Stress Shadows on Near-Trench Coupling. *Geophysical Research Letters* **45**, 4754–4763 (2018).

31. Ader, T. *et al.* Convergence rate across the Nepal Himalaya and interseismic coupling on the Main Himalayan Thrust: Implications for seismic hazard. *Journal of Geophysical Research: Solid Earth* **117**, (2012).

32. Dal Zilio, L., Jolivet, R. & van Dinther, Y. Segmentation of the Main Himalayan Thrust Illuminated by Bayesian Inference of Interseismic Coupling. *Geophysical Research Letters* **47**, e2019GL086424 (2020).

33. Jouanne, F., Mugnier, J. L., Sapkota, S. N., Bascou, P. & Pecher, A. Estimation of coupling along the Main Himalayan Thrust in the central Himalaya. *Journal of Asian Earth Sciences* **133**, 62–71 (2017).

34. Li, S. *et al.* Interseismic Coupling beneath the Sikkim–Bhutan Himalaya Constrained by GPS Measurements and Its Implication for Strain Segmentation and Seismic Activity. *Remote Sensing* **12**, 2202 (2020).

35. Lindsey, E. O. *et al.* Structural Control on Downdip Locking Extent of the Himalayan Megathrust. *Journal of Geophysical Research: Solid Earth* **123**, 5265–5278 (2018).

36. Panda, D. & Lindsey, E. O. Overriding Plate Deformation Controls Inferences of Interseismic Coupling Along the Himalayan Megathrust. *JGR Solid Earth* **129**, e2024JB029819 (2024).

37. Stevens, V. L. & Avouac, J. P. Interseismic coupling on the main Himalayan thrust. *Geophysical Research Letters* **42**, 5828–5837 (2015).

38. Ellis, A. *et al.* GPS constraints on deformation in northern Central America from 1999 to 2017, Part 2: Block rotations and fault slip rates, fault locking and distributed deformation. *Geophysical Journal International* **218**, 729–754 (2019).

39. Hanifa, N. R. *et al.* Interplate coupling model off the southwestern coast of Java, Indonesia, based on continuous GPS data in 2008–2010. *Earth and Planetary Science Letters* **401**, 159–171 (2014).

40. Widiyantoro, S. *et al.* Implications for megathrust earthquakes and tsunamis from seismic gaps south of Java Indonesia. *Sci Rep* **10**, 15274 (2020).

41. Hayes, G. P. The finite, kinematic rupture properties of great-sized earthquakes since 1990. *Earth and Planetary Science Letters* **468**, 94–100 (2017).

42. Wong, J. W. C., Fan, W. & Gabriel, A.-A. A Quantitative Comparison and Validation of Finite-Fault Models: The 2011 Tohoku-Oki Earthquake. *Journal of Geophysical Research: Solid Earth* **129**, e2024JB029212 (2024).

43. Ammon, C. J., Lay, T., Kanamori, H. & Cleveland, M. A rupture model of the 2011 off the Pacific coast of Tohoku Earthquake. *Earth Planet Sp* **63**, 33 (2011).

44. Fujii, Y., Satake, K., Sakai, S., Shinohara, M. & Kanazawa, T. Tsunami source of the 2011 off the Pacific coast of Tohoku Earthquake. *Earth Planet Sp* **63**, 815–820 (2011).

45. Gusman, A. R., Tanioka, Y., Sakai, S. & Tsushima, H. Source model of the great 2011 Tohoku earthquake estimated from tsunami waveforms and crustal deformation data. *Earth and Planetary Science Letters* **341–344**, 234–242 (2012).

46. Ide, S., Baltay, A. & Beroza, G. C. Shallow Dynamic Overshoot and Energetic Deep Rupture in the 2011 Mw 9.0 Tohoku-Oki Earthquake. *Science* **332**, 1426–1429 (2011).

47. Lay, T., Ammon, C. J., Kanamori, H., Xue, L. & Kim, M. J. Possible large near-trench slip during the 2011 Mw 9.0 off the Pacific coast of Tohoku Earthquake. *Earth Planet Sp* **63**, 32 (2011).

48. Satake, K., Fujii, Y., Harada, T. & Namegaya, Y. Time and Space Distribution of Coseismic Slip of the 2011 Tohoku Earthquake as Inferred from Tsunami Waveform Data. *Bulletin of the Seismological Society of America* **103**, 1473–1492 (2013).

49. Shao, G., Li, X., Ji, C. & Maeda, T. Focal mechanism and slip history of the 2011 Mw 9.1 off the Pacific coast of Tohoku Earthquake, constrained with teleseismic body and surface waves. *Earth Planet Sp* **63**, 559–564 (2011).

50. Wei, S., Graves, R., Helmberger, D., Avouac, J.-P. & Jiang, J. Sources of shaking and flooding during the Tohoku-Oki earthquake: A mixture of rupture styles. *Earth and Planetary Science Letters* **333–334**, 91–100 (2012).

51. Yagi, Y. & Fukahata, Y. Rupture process of the 2011 Tohoku-oki earthquake and absolute elastic strain release. *Geophysical Research Letters* **38**, (2011).

52. Yamazaki, Y., Lay, T., Cheung, K. F., Yue, H. & Kanamori, H. Modeling near-field tsunami observations to improve finite-fault slip models for the 11 March 2011 Tohoku earthquake. *Geophysical Research Letters* **38**, (2011).

53. Yue, H. & Lay, T. Source Rupture Models for the Mw 9.0 2011 Tohoku Earthquake from Joint Inversions of High‐Rate Geodetic and Seismic Data. *Bulletin of the Seismological Society of America* **103**, 1242–1255 (2013).

54. Delouis, B., Nocquet, J.-M. & Vallée, M. Slip distribution of the February 27, 2010 Mw = 8.8 Maule Earthquake, central Chile, from static and high-rate GPS, InSAR, and broadband teleseismic data. *Geophysical Research Letters* **37**, (2010).

55. Lorito, S. *et al.* Limited overlap between the seismic gap and coseismic slip of the great 2010 Chile earthquake. *Nature Geosci* **4**, 173–177 (2011).

56. Luttrell, K. M., Tong, X., Sandwell, D. T., Brooks, B. A. & Bevis, M. G. Estimates of stress drop and crustal tectonic stress from the 27 February 2010 Maule, Chile, earthquake: Implications for fault strength. *Journal of Geophysical Research: Solid Earth* **116**, (2011).

57. Pollitz, F. F. *et al.* Coseismic slip distribution of the February 27, 2010 Mw 8.8 Maule, Chile earthquake. *Geophysical Research Letters* **38**, (2011).

58. Radiguet, M. *et al.* Slow slip events and strain accumulation in the Guerrero gap, Mexico. *Journal of Geophysical Research: Solid Earth* **117**, (2012).

59. Loveless, J. P. & Meade, B. J. Two decades of spatiotemporal variations in subduction zone coupling offshore Japan. *Earth and Planetary Science Letters* **436**, 19–30 (2016).

60. Wallace, L. M. Slow Slip Events in New Zealand. *Annu. Rev. Earth Planet. Sci.* **48**, 175–203 (2020).

61. Maubant, L., Frank, W. B., Wallace, L. M., Williams, C. A. & Hamling, I. Imaging the Spatiotemporal Evolution of Plate Coupling With Interferometric Radar (InSAR) in the Hikurangi Subduction Zone. *Geophysical Research Letters* **50**, e2023GL105388 (2023).

62. Uphoff, C., May, D. A. & Gabriel, A.-A. A discontinuous Galerkin method for sequences of earthquakes and aseismic slip on multiple faults using unstructured curvilinear grids. *Geophysical Journal International* **233**, 586–626 (2023).

63. Lotto, G. C., Jeppson, T. N. & Dunham, E. M. Fully Coupled Simulations of Megathrust Earthquakes and Tsunamis in the Japan Trench, Nankai Trough, and Cascadia Subduction Zone. *Pure Appl. Geophys.* **176**, 4009–4041 (2019).

64. Oryan, B. *et al.* Megathrust locking encoded in subduction landscapes. *Science Advances* **10**, eadl4286 (2024).